Motion Response Characteristics of a Kyushu-University Semi- Submersible Floating Wind Turbine with Trussed Slender Structures: Experiment vs. Numerical Simulation

Liu, Yingyi
Research Institute for Applied Mechanics, Kyushu University

Hu, Changhong
Research Institute for Applied Mechanics, Kyushu University

Sueyoshi, Makoto
Research Institute for Applied Mechanics, Kyushu University

Yoshida, Shigeo
Research Institute for Applied Mechanics, Kyushu University

他

https://hdl.handle.net/2324/4743304

1 # Motion Response Characteristics of a Kyushu-University Semi-Submersible Floating Wind Turbine with Trussed Slender Structures: Experiment vs. Numerical Simulation

4 *Yingyi Liu [a],*, Changhong Hu [a], Makoto Sueyoshi [a], Shigeo Yoshida [a], Hidetsugu Iwashita [b],*
5 *Masashi Kashiwagi [c]*

6 *[a] Research Institute for Applied Mechanics, Kyushu University, Fukuoka, 8168580, Japan*
7 *[b] Department of Transportation and Environmental Systems, Hiroshima University, Hiroshima, 7398527, Japan*
8 *[c] Department of Naval Architecture & Ocean Engineering, Osaka University, Osaka, 5650871, Japan*

9 Emails: *liuyingyi@riam.kyushu-u.ac.jp (Y. Liu); hu@riam.kyushu-u.ac.jp (C. Hu); sueyoshi@riam.kyushu-u.ac.jp (M.*
10 *Sueyoshi); yoshidas@riam.kyushu-u.ac.jp (S. Yoshida); iwashita@naoe.hiroshima-u.ac.jp (H. Iwashita);*
11 *kashi@naoe.eng.osaka-u.ac.jp (M. Kashiwagi)*
12
13 ***** Correspondence e-mail: liuyingyi@riam.kyushu-u.ac.jp; Tel.: +81-80-8565-7934

15 **Abstract:** Understanding the dynamics of an FWT (Floating Wind Turbine) is essential for its design and
16 operation. Since a truss structure can reduce the wave load/resistance on the floating foundation, it becomes
17 more and more popular in industrial applications. In this regard, knowing the effect of slender members of the
18 truss structure on the motion response characteristics of such an FWT is vital. The present work develops a
19 time-domain method for modeling the dynamics of a floating truss-structure wind turbine with multiple rotors
20 on the deck of the platform. In its hydrodynamic aspect, a hybrid panel-stick model is built up incorporating
21 the potential flow theory to calculate the wave inertia force and a Morison strip method to calculate the wave
22 drag force. A systematic methodology, and the corresponding efficient tool, have been developed to deal with
23 the floating truss-structure consisting of a set of slender cylindrical members in arbitrary lengths, diameters,
24 orientations, and locations. The Morison dynamic solver is incorporated into the time-domain solver for the
25 FWT dynamics. The proposed model is validated against a model experiment of a semi-submersible FWT with
26 a triangular-shaped truss-structured platform, which was carried out in RIAM (Research Institute for Applied
27 Mechanics), Kyushu University. Good agreements between the simulation results and the experimental data
28 confirm the validity of the developed method. Further numerical simulations are performed in a set of wind
29 and wave conditions to investigate the effect of wave drag force on the FWT dynamics. It is found that without
30 the fluid viscosity, resonant responses are excited in the platform motions at frequencies that are close to the
31 natural frequencies of the FWT system. Via a comparison between the parked conditions and operating
32 conditions of the FWT, it is found that in the presence of steady wind, the translational surge or sway motion
33 is significantly excited at its resonance frequency. This may be attributed to the work done by the wind to the
34 FWT, which enhances remarkably the total kinetic energy of the platform and consequently increases the
35 translational surge or sway velocity of the platform at the equilibrium position. Applying a hybrid panel-stick
36 model will be effective in reducing all these non-realistic large resonant responses.

37 **Keywords:** trussed structure; slender bracings; catenary mooring system; viscous damping; motion response
38 analysis; hybrid model.
39
40

1. Introduction

Offshore wind turbine offers a promising solution to harnessing the abundant wind resources. With the development of technology, the offshore wind turbine industry is gradually moving from shallow water to intermediate water and deepwater. As one of the three mainstream concepts of the floating foundation to keep stability, the semi-submersible type has a smaller surge response than the TLP (Tension Leg Platform) type and a smaller pitch response than the spar type (Li et al., 2011; Goupee et al., 2014). The installation cost of the mooring system of a semi-submersible foundation is also relatively lower than the other types of floating foundations (Liu et al., 2016c).

As a consequence, in the past decade, several important configurations of the semi-submersible type have been proposed, e.g., the WindFloat™ (Roddier et al., 2010), DeepCwind (Robertson et al., 2014), WINFLO™ (Boulluec et al., 2013), etc. Researches have been undertaken on various aspects of the semi-submersible concept, involving model testing (Robertson et al., 2017; Kim et al., 2017; Li et al., 2018; Koch et al., 2018), numerical modeling and conceptual study (Bae et al., 2014; Bayati et al., 2014; Karimirad and Michailides, 2015 and 2016; Liu et al., 2018) as well as other aspects relevant to the uncertainty analysis, the control design, and the fatigue prevention, etc. (Zhu et al., 2016; Wang et al., 2016; Uzunoglu et al., 2018; Liu et al., 2018). Typically, these semi-submersible foundations have three or four columns to provide the main buoyancy force and some other small, slender members to support the stiffness of the entire structure.

An important issue of the semi-submersible foundations is the prediction of their motion responses, among which the heave response may be of particular concern. At a special frequency, i.e., the near-zero-excitation frequency, the wave excitation force can almost disappear at the equilibrium position during the heave motion. Faltinsen (1990) stated that in beam seas, the heave natural frequency should be larger than its near-zero-excitation frequency. This conclusion was later confirmed by Newman (1999). Newman (1999) also proved that in the long-wavelength regime, the heave RAO (Response Amplitude Operator) approaches unity. At the natural frequencies, when using a potential flow-based method, the semi-submersible normally endures remarkable resonant responses. The reason lies in that, in fact, near the boundary layer of the submerged part of the floating structure, the wave-induced drag force (which is a viscous force) has not been accounted for as that is usually done in an N-S (Navier-Stokes) equation-based solver. Expected discrepancies can be found in the computation results of the 6-DoF (Degree of Freedom) motion responses of an FWT between a potential flow-based method and a CFD (Computational Fluid Dynamics) method (Nematbakhsh et al., 2015).

To include the viscous effect, the potential flow-based method needs to be modified to some extent. Sarpkaya (2015) investigated the relative dominant wave loading regimes for a circular cylinder, which was also listed in Benitz et al. (2015), and discovered that the wave diffraction theory is only strictly valid for the region of $\pi D/L < 0.5$ (in which D is the diameter of the cylinder and L is the wavelength); outside of this region, the wave drag force needs to be considered. Other than solving the N-S equation, which is extremely time-consuming and cost-expensive, an alternative way is to employ a hybrid approach combing the potential flow theory and the Morison equation (Li and Yu, 2012). A list of numerical methods is given in Table 1, which are primarily based on the potential flow theory and the Morison equation, with the aid of various modeling tools. These methods apply various hybrid methodologies for modeling the hydrodynamics of the floating platform, taking into consideration where to account for the diffraction-radiation effect and where to account for the viscous effect. By performing numerical simulations for different concepts of semi-submersible FWTs, almost all of these researches confirmed that inclusion of the Morison counterpart as a supplement to the potential flow-based methods could result in more reasonable predictions for the dynamic responses of semi-submersible FWTs, especially those having plenty of slender bracings.

90

Table 1. A review of numerical methods for modeling a semi-submersible FWT

Authors	Potential Flow Method	Morison Method	Hybrid Methodology	FWT Modeling Software	FWT Model
Kvittem et al. (2012)	BEM (WADAM™)	Time domain	BEM for all members (inertia), Morison for some members (drag)	SIMO™/RIFLEX™	FWT similar to WindFloat™
Ledru et al. (2014)	BEM (Diodore™)	Time domain	BEM for columns (inertia), Morison for the other members (inertia + drag)	DeepLines™	OC4 DeepCwind FWT©
Tran & Kim (2015)	BEM (AQWA™)	Time domain	BEM for columns and plates (inertia), Morison for bracings (drag)	AQWA-Line™ /AQWA-NAUT™	OC4 DeepCwind FWT©
Wendt et al. (2015)	BEM (WAMIT™)	Time domain	BEM for all members (inertia), Morison for all members (drag)	HydroDyn© /FAST©	OC4 DeepCwind FWT©
Liu et al. (2015)	BEM (HAMS©)	Frequency domain	Two hybrid modeling strategies were introduced and compared	-	Kyushu-University FWT©
Ishihara & Zhang (2019)	-	Time domain	Morison for all members (inertia + drag)	inhouse code	Not mentioned
Present method	BEM (HAMS©)	Time domain	BEM for all members (inertia), Morison for all members (drag)	inhouse code	Kyushu-University FWT©

91

The Morison equation can be easily applied to a monopile or Spar because of its simple regular geometry. However, in respect to a complex truss structure with a great number of braces, as shown in Figure 1, unlike the braceless type (e.g., Karimirad and Michailides, 2015; 2016), one needs to develop a systematic methodology to take into consideration of all geometric specifications, i.e., the diameters, lengths, orientations, and locations of all members. It may involve the development of a Morison mesh generator and a Morison dynamic solver. Based on the study in Liu et al. (2015), an appropriate way of hybrid modeling is to apply BEM (Boundary Element Method) for the inertia part of wave force while using the Morison method for the drag part on all the members. Such a way can substantially improve the computation efficiency but avoid double-counting the fluid inertia and the wave excitation (Tran & Kim, 2015). Besides, although many of the previous researches studied the effect of viscous wave loading on the floating platform of an FWT in parked status, rare research concerns the impact of viscous wave loading on the platform under the circumstance of FWT operation. Indeed, it is crucial to investigate the role that the wave drag force takes in affecting the motion of an FWT in the presence of wind. In particular, whether wind matters or not in this process and what is the specific role of wind need to be understood as clearly as possible. For this purpose, the present work tries to fulfill this gap and answer the above questions.

The present work focuses on the prediction and analysis of the motion responses of such a complex semi-submersible with truss members and the understanding of its associated phenomena. A time-domain method is going to be developed to simulate a multi-rotor FWT system, which involves a newly developed hybrid panel-stick method using the strategy mentioned above. Wake effect from the upstream wind turbine will also be considered by using Jensen's model (Jensen, 1983; Katic et al., 1986). Following a validation with the experimental model test, a systematic investigation using the numerical method will be undertaken to study the role of the wave drag force on the semi-submersible FWT with and without the existence of wind. Conclusions will consequently be drawn based on the preceding analysis.

2. The Prototype FWT in Kyushu University

In recent years, a multi-rotor FWT has been proposed in Kyushu University, which is one of the projects in the spotlight in Japan. In the design, a number of slender cylindrical braces are included

120   to reduce the high wave loading as well as to bring down the cost. To maximize the absorption of the
121   wind power, three wind turbines are installed atop the primary columns of the floating foundation
122   (Hu et al., 2014; Liu et al., 2016). As a multi-purpose floating marine renewable energy system, solar
123   panels are simultaneously installed at its large-space deck, as shown in Figure 1, from which the
124   generated electricity can be used by the surrounding aquaculture farm as well. The layout of the
125   mooring system and the definition of the coordinate system are displayed in Figure 2. Specifications
126   of the prototype are listed in Table 2.

127
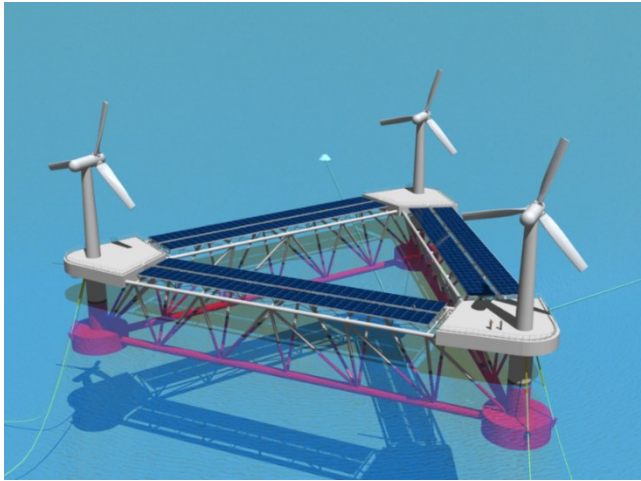
128   **Figure 1.** 3D computer graph of a triangular offshore renewable energy system developed in Kyushu
129   University. Slender truss braces are used to strengthen the floating structure and reduce the wave
130   loading acting upon the platform.

131
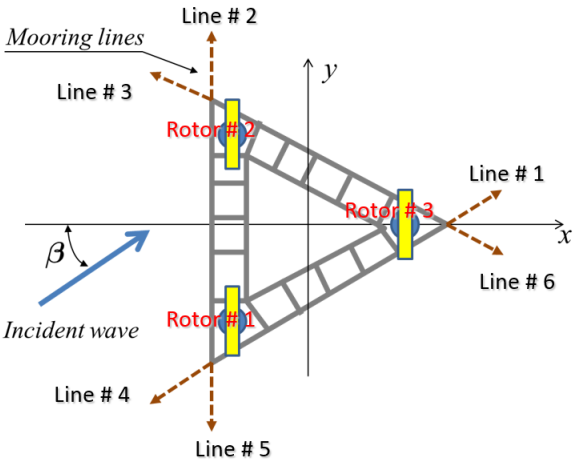
132   **Figure 2.** The layout of the mooring system of the semi-submersible FWT. The origin of the coordinate
133   system for the subsequent analysis locates at the planar center of the triangular platform at MSL
134   (Mean Sea Level).

135   **Table 2.** Definition of full-scale properties of the semi-submersible

Rotor Diameter	23.38 m
Rated Power for Each Turbine	350 kW
Hub Height above MSL	33.00 m
Platform Mass	2.17×10^6 kg
Mass of Tower and Nacelle for Each Turbine	9.25×10^4 kg

Total Draft	10.00 m
Platform Displacement	$2.12 \times 10^3 \, \text{m}^3$
Number of Mooring Lines	6
Angle between Adjacent Lines	60.00 degree
Water Depth (Depth of Anchor)	70.00 m
Depth of Fairlead below MSL	7.00 m
Radius to Anchor from Fairlead	200.00 m
Radius to Fairlead from CM	51.96 m
Unstretched Mooring Line Length	200.00 m
Mooring Line Diameter	0.06 m
Equivalent Mooring Line Mass Density	68.6 kg/m
Equivalent Mooring Line Stiffness	$1.38 \times 10^6 \, \text{N}$

136

3. Time Domain Simulation Method for a Floating Offshore Wind Turbine System

3.1. Motion Equation of the Semisubmersible in Time Domain

In the aforementioned FWT system, wave force and wind force are generally the two main external dynamic forces which the system experiences throughout the entire operation lifetime. Besides, as a major source of the restoring force, the mooring tension loads can keep the floating system from being drifted away under the action of waves and winds. Since the members of the structure are of small aspect ratios, viscous loading in the form of drag force also serves an important role in restraining the motion response, especially in the neighborhood of the resonant periods of the system. Therefore, the motion time history for the integrated floating system can be described by the following equation based on the work of Jonkman (2007):

$$[M_{ij} + A_{ij}(\infty)]\ddot{\xi}_j(t) + \int_0^t K_{ij}(t-\tau)\dot{\xi}_j(\tau)d\tau + C_{ij}\xi_j(t)$$

$$= F_i^{Wind}(t) + F_i^{Wave}(t) + F_i^{Mooring}(t) + F_i^{Viscous}(t), \ (i,j = 1 \sim 6), \tag{1}$$

where M_{ij}, C_{ij} are the mass matrix and the restoring matrix of the floating body, respectively; K_{ij} is the retardation function that can be calculated through the cosine transformation of the damping coefficient $B_{ij}(\omega)$

$$K_{ij}(t) = \frac{2}{\pi} \int_0^\infty B_{ij}(\omega) \cos \omega t \, d\omega, \tag{2}$$

$A_{ij}(\infty)$ is the infinite-frequency limit of the added mass $A_{ij}(\omega)$

$$A_{ij}(\infty) = A_{ij}(\omega) + \frac{1}{\omega} \int_0^\infty K_{ij}(t) \cos \omega t \, dt, \tag{3}$$

The Filon quadrature method (Xiang, 2007)) is chosen to compute the Fourier integrals with good accuracy. The forces at the right-hand side of Eq. (1) correspond to the wind loads, the wave excitation loads, the mooring tension loads, and the viscous loads, respectively. The hydrodynamic quantities can be solved by a standard frequency-domain solver (Liu et al., 2018a; 2019), based on the assumption that the fluid is incompressible, irrotational, and inviscid. The hydrodynamic wave excitation loads acting on the floating platform in the time domain can, therefore, be represented by a convolution of the wave

159 elevation and the non-causal impulse response function, where the latter is determined by the Fourier
160 transform of the wave excitation forces in the frequency domain (Liu et al., 2014).
161   The mooring tension loads are found at each time step by the solution of an extended catenary
162 theory (Jonkman, 2009) via the Newton-Raphson iteration method, which is capable of considering the
163 seabed friction to the mooring lines. Due to the small diameters of the cylindrical structures of the
164 complex platform in comparison to the wavelength, it is essential to include a supplemental model to
165 account for the viscous correction for the potential flow theory. A Morison-stick model was therefore
166 formulated in the frequency domain (Liu et al., 2016), and is reformulated here in the time domain
167 (Section 4.1 and 4.2).

168 *3.2. Aerodynamics of the Multiple Rotors*

169   The BEMT (Blade Element Momentum Theory), which assumes that the blades can be divided
170 into small annular elements that operate aerodynamically as two-dimensional airfoils (Moriarty and
171 Hansen, 2005), is applied to the aerodynamics computation of each rotor. The crucial step of the
172 BEMT is to find the axial induction factor and the tangential induction factor via a standard iterative
173 procedure. Let the thrust load derived respectively from the momentum theory and the blade
174 element theory be equalized, the axis induction factor a and the tangential induction factor a' can
175 be therefore deduced as follows

$$a = 1 \Big/ \left(1 + \frac{4F \sin^2 \varphi}{\sigma C_n} \right), \tag{4}$$

$$a' = 1 \Big/ \left[-1 + \frac{4F \sin \varphi \cos \varphi}{\sigma C_t} \right], \tag{5}$$

176 where F is the product of the tip-loss factor and the hub-loss factor, C_n and C_t are the lift and the drag
177 coefficients of a local blade element, φ is the local flow angle, and σ is the local solidity. To
178 compensate for the deficiency when the rotor enters into the turbulent wake state, the Glauert
179 correction (Spera, 1994) is employed. After resolving the distribution of the normal and the tangential
180 loads along the span of blades, the total thrust force and the shaft torque are obtained by integrations
181 assuming a linear variation (Hansen, 2008) of the load distribution between neighboring blade
182 elements.
183   Note that there exist multiple rotors on the deck of the semi-submersible floating foundation,
184 and the interactions between the rotors can significantly affect the loadings from the wind. To reflect
185 this phenomenon efficiently, the Jensen's wake model (Jensen, 1983; Katic et al., 1986), also known as
186 the 'Park model', is utilized in the present study. Its empirical equation is based on the conservation
187 of momentum to model a single wake. It is valid for the downstream distance approximately above
188 one rotor diameter in the far wake region. The wind speed in the wake can be expressed as

$$U_w(x) = U_\infty \left(1 - \frac{1 - \sqrt{1 - C_{T,b}}}{(1 + 2k_w x / D_{rotor})^2} \right), \tag{6}$$

189 where D_{rotor} is the rotor diameter, k_w is the wake decay constant, and x is the distance behind the
190 upstream rotor. Typical values for k_w range from 0.04 for offshore (Barthelmie et al., 2010) to 0.075
191 for onshore cases (Barthelmie et al., 2005). The wake decay constant sets the linear rate of wake
192 expansion with the distance in the streamwise direction. The diameter of the wake expansion is
193 therefore given by

$$D_w = D_{rotor} + 2k_w x. \tag{7}$$

194 *3.3. Modeling of the Catenary Mooring System*

195   In mild sea conditions, the mooring line dynamics can often be described by a linearized
196 relationship to the displacement of the floating support platform. In general, however, the mooring
197 system dynamics are not linear. Instead, nonlinearities are generally evident in the force-displacement

relationships. For the semi-submersible FWT, as shown in Figure 1, the application of an appropriate catenary theory is necessary. Because the traditional catenary theory could not explain the effect of the seabed interaction with a mooring cable in the case it touches the seabed, an improved method proposed by Jonkman (2009) is used in this work, which is capable of accounting for the above issue.

The analytical model, which is given in terms of two unknown variables, i.e., the horizontal and the vertical components of the effective tension in each mooring line at the fairlead, is formulated as follows

$$x_F(F_H, F_V) = L - \frac{F_V}{w} + \frac{F_H}{w} ln\left[\frac{F_V}{F_H} + \sqrt{1 + \left(\frac{F_V}{F_H}\right)^2}\right] + \frac{F_H L}{EA} + \frac{C_B w}{2EA}\left[-\left(L - \frac{F_V}{w}\right)^2 + \left(L - \frac{F_V}{w} - \frac{F_H}{C_B w}\right) MAX\left(L - \frac{F_V}{w} - \frac{F_H}{C_B w}, 0\right)\right], \tag{8}$$

$$z_F(F_H, F_V) = \frac{F_H}{w}\left[\sqrt{1 + \left(\frac{F_V}{F_H}\right)^2} - \sqrt{1 + \left(\frac{F_V - wL}{F_H}\right)^2}\right] + \frac{1}{EA}\left(F_V L - \frac{wL^2}{2}\right), \tag{9}$$

where x_F and z_F are respectively the horizontal and vertical coordinates of the fairlead position relative to the anchor, F_H and F_V are the horizontal and vertical components of the effective tension in the mooring line at the fairlead, w is the mass of the mooring line per unit length, L is the total unstretched mooring line length, C_B is the drag coefficient of seabed static-friction, and EA is the sectional stiffness of the mooring line. It is worth noting that Equations (8) and (9) should be solved iteratively in the local coordinate system via the Newton–Raphson method, etc.

3.4. Solution of the Time-Domain Motion Equation

Several numerical integration methods can solve a differential equation of the second order in the time domain, such as the Newmark-Beta scheme (Wikipedia, 2020a), Adams-Moulton scheme (Wikiversity, 2020b), Adams-Bashforth scheme (Wikiversity, 2020b) and Runge-Kutta scheme (Wikipedia, 2020c). Herein the fourth-order Runge-Kutta scheme is selected to find the solution of Eq. (1) as it can acquire as more as enough accuracy (Ran, 2000; Li and Teng, 2002). Let us consider the time-domain motion equation in the form of $\{\ddot{\xi}\} = Q[t, \{\xi\}, \{\dot{\xi}\}]$, i.e.,

$$Q[t, \{\xi(t)\}, \{\dot{\xi}(t)\}] = [\boldsymbol{M} + \boldsymbol{A}]^{-1}\left\{-\int_0^t [\boldsymbol{K}(t - \tau)]\{\dot{\xi}(\tau)\}d\tau - [\boldsymbol{C}]\{\xi(t)\} + \{F^{Wind}(t)\} + \{F^{Wave}(t)\} + \{F^{Mooring}(t)\} + \{F^{Viscous}(t)\}\right\}, \tag{10}$$

where a letter in bold represents a matrix, and $\{\cdot\}$ represents a vector. The solutions at each time step can be found via the fourth-order Runge-Kutta scheme as the following

$$\{\xi(t + \Delta t)\} = \{\xi(t)\} + \Delta t \cdot \{\dot{\xi}(t)\} + \Delta t \cdot (Q_1 + Q_2 + Q_3)/6, \tag{11}$$

$$\{\dot{\xi}(t + \Delta t)\} = \{\dot{\xi}(t)\} + (Q_1 + 2Q_2 + 2Q_3 + Q_4)/6, \tag{12}$$

where

$$Q_1 = \Delta t \cdot Q[t, \{\xi(t)\}, \{\dot{\xi}(t)\}], \tag{13}$$

$$Q_2 = \Delta t \cdot Q[t + \Delta t/2, \{\xi(t)\} + \Delta t \cdot \{\dot{\xi}(t)\}/2, \{\dot{\xi}(t)\} + Q_1/2], \tag{14}$$

$$Q_3 = \Delta t \cdot Q[t + \Delta t/2, \{\xi(t)\} + \Delta t \cdot \{\dot{\xi}(t)\}/2 + \Delta t \cdot Q_1/4, \{\dot{\xi}(t)\} + Q_2/2], \tag{15}$$

$$Q_4 = \Delta t \cdot Q[t + \Delta t, \{\xi(t)\} + \Delta t \cdot \{\dot{\xi}(t)\} + \Delta t \cdot Q_2/2, \{\dot{\xi}(t)\} + Q_3]. \tag{16}$$

4. A Morison-Stick Method for Modeling Floating Truss Structures in Time Domain

4.1. Theory, Formulation and Numerical Implementation of the Morison-Stick Method

223   The viscous effect plays an important role in the dynamic response of such a semi-submersible
224   since the diameters of the slender braces are small in comparison to the wavelengths in a typical sea
225   condition. A Morison-type method is necessary to be employed in combination with the potential
226   flow theory. Based on the conclusion of Liu et al. (2016), an appropriate hybrid approach can apply a
227   Morison method in the calculation of the wave drag force and a potential flow theory-based method
228   in the calculation of the platform inertia force. Such a combination can lead to the high accuracy of
229   prediction. This concept will be applied as well to the present time-domain method.

230   Following Leblanc et al. (1993), the wave drag force upon a cylindrical member can be obtained
231   via the integration along its length, i.e.,

$$\vec{F}_D = \frac{1}{2}\rho C_D \int_s^e D_{mem} V_{rT} \vec{V}_{rT} dl \,, \tag{17}$$

232   where C_D, D_{mem} and l are respectively the drag coefficient, the diameter and the length of a
233   cylindrical member, ρ is the water density, V_{rT} is the absolute value of $\vec{V}_{rT}$ which is the transverse
234   component of the wave-body relative velocity $\vec{V}_r$. Besides, "s" and "e" represent the start and the end
235   of a cylindrical member, respectively. The wave-body relative velocity $\vec{V}_r$ is the difference between
236   the wave-particle velocity $\vec{V}_w$ and the motion velocity of a floating structure $\vec{V}_m$, i.e.,

$$\vec{V}_r = \vec{V}_w - \vec{V}_m. \tag{18}$$

237   It is easy to know, the floating structure motion at the centroid of a Morison element can be calculated
238   as

$$\vec{V}_m = \left(\dot{\xi}_1,\dot{\xi}_2,\dot{\xi}_3\right)^t + \left(\dot{\xi}_4,\dot{\xi}_5,\dot{\xi}_6\right)^t \times \vec{R} = \boldsymbol{P}\vec{V}_g \tag{19}$$

239   where $\dot{\xi}_i$ ($i = 1\sim6$) represents the platform motion velocity in the ith DoF, $\vec{R} = \left(x - x_g, y - y_g, z - \right.$
240    $\left. z_g\right)^t$ represents the position vector of the Morison element in the body-fixed system (the superscript
241   "t" means "transpose" of the vector), $\vec{V}_g = \left(\dot{\xi}_1,\dot{\xi}_2,\dot{\xi}_3,\dot{\xi}_4,\dot{\xi}_5,\dot{\xi}_6\right)^t$ is the platform velocity vector at the
242   gravity center of the floating structure, and $\boldsymbol{P}$ stands for the following translational-to-rotational
243   transformation matrix

$$\boldsymbol{P} = \begin{bmatrix} 1 & 0 & 0 & 0 & z - z_g & -(y - y_g) \\ 0 & 1 & 0 & -(z - z_g) & 0 & x - x_g \\ 0 & 0 & 1 & y - y_g & -(x - x_g) & 0 \end{bmatrix}. \tag{20}$$

244   Based on the principle of the double vector product, the transverse component $\vec{V}_T$ of a velocity vector
245    $\vec{V}$ can be expressed by

$$\vec{V}_T = \vec{l} \times \vec{V} \times \vec{l} = \vec{V} - \left(\vec{V} \cdot \vec{l}\right)\vec{l} = \boldsymbol{T}\vec{V} \tag{21}$$

246   where $\vec{l} = \left(l_x, l_y, l_z\right)$ is the unit vector along the axial direction of the cylindrical member to which
247   the Morison element belongs, and $\boldsymbol{T}$ is the axial-to-transverse transformation matrix that is calculated
248   by

$$\boldsymbol{T} = \boldsymbol{I} - \vec{l}\vec{l}^t = \begin{bmatrix} 1 - l_x^2 & -l_x l_y & -l_x l_z \\ -l_y l_x & 1 - l_y^2 & -l_y l_z \\ -l_z l_x & -l_z l_y & 1 - l_z^2 \end{bmatrix}, \tag{22}$$

249   where $\boldsymbol{I}$ stands for the 3-order Identity Matrix. Taking into consideration simultaneously Eqs. (18) ~
250   (22), the transverse component of the relative water velocity can be expressed by

$$\vec{V}_{rT} = \boldsymbol{T}\vec{V}_w - \boldsymbol{T}\boldsymbol{P}\vec{V}_g, \tag{23}$$

251   and the wave drag force upon a segment of a cylindrical member can be written as

$$\vec{F}_D^{i,j} = \frac{1}{2}\rho C_D^i D_{mem}^i (\delta l)^{i,j} \left| T^{i,j}\vec{V}_w^{i,j} - T^{i,j}P^{i,j}\vec{V}_g \right| \left(T^{i,j}\vec{V}_w^{i,j} - T^{i,j}P^{i,j}\vec{V}_g \right), \tag{24}$$

$$\vec{M}_D^{i,j} = \vec{R}^{i,j} \times \frac{1}{2} \rho C_D^i D_{mem}^i (\delta l)^{i,j} \left| T^{i,j} \vec{V}_w^{i,j} - T^{i,j} P^{i,j} \vec{V}_g \right| \left(T^{i,j} \vec{V}_w^{i,j} - T^{i,j} P^{i,j} \vec{V}_g \right). \tag{25}$$

252   where the superscripts 'i, j' stand for the jth Morison segment of the ith cylindrical member.
253   Therefore, the viscous force at the right-hand side of Eq. (1) can be finally deduced in the following
254   form

$$\vec{F}^{Viscous}(t) = \sum_{i=1}^{N_{mem}} \sum_{j=1}^{N_{seg}^i} (P^{i,j})^t \times \vec{F}_D^{i,j}. \tag{26}$$

255   where N_{mem} represents the number of all cylindrical members and N_{seg}^i represents the number of
256   Morison segments on the ith cylindrical member. Upon each tubular member, the local incident wave
257   kinematics, as mentioned in Section 4.2, is used to calculate its quadratic wave drag force in either a
258   regular wave or irregular waves by the Morison dynamic solver. The vector $\vec{F}^{Viscous}$ is then
259   calculated at every time step with the present displacement and the motion velocity of the floating
260   structure. Thereafter, by resolving the time domain motion equation Eq. (10), the displacement and
261   the motion velocity of the floating structure can be updated for the calculation at the next time step.
262   In respect of the numerical implementation of the wave drag model, a Morison-stick mesh
263   generator is specially developed to generate the stick mesh. As shown in Figure 3, the hybrid mesh
264   is created for the immersed part of the floating structure under the mean water level. The number of
265   Morison segments on each of the cylindrical members can be set at the users' discretion in advance.
266   In the stick-mesh generator, the location and affiliation of each Morison segment on each of the
267   cylindrical members, the equivalent cross-section diameter, the axis length, the axis direction, and
268   the drag coefficients C_D of each cylindrical member, are recorded into the generated stick mesh as
269   an input file to the time-domain solver.

270
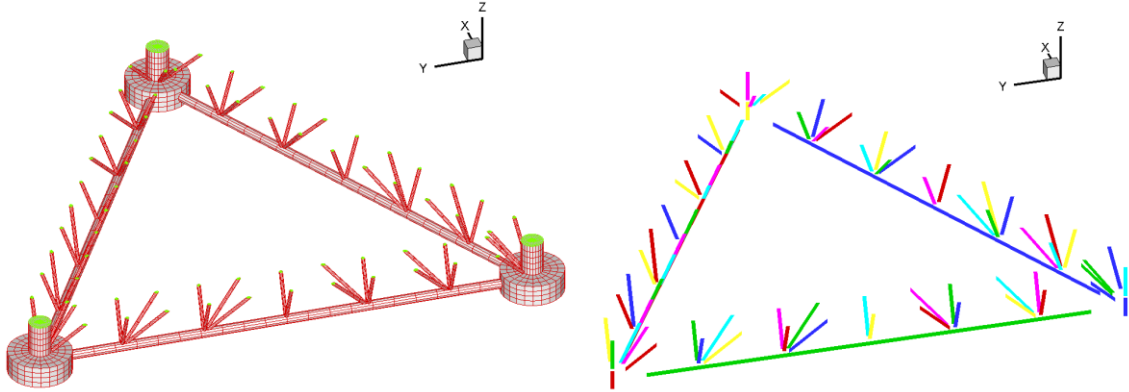
271   **Figure 3.** A hybrid panel-stick model for the floating truss structure: (a) a panel mesh for calculation
272   of the wave inertia forces using the potential flow method; (2) a stick mesh for calculation of the wave
273   drag force using the Morison method.

274   *4.2. Fluid Kinematics of Incident Waves in Regular and Irregular Waves*

275   Considering an Airy wave transmitting with a small amplitude A and an angular frequency w,
276   in the water with a finite depth of h, the incident wave potential for this regular wave at any position
277   (x,y,z) can be described by

$$\Phi(x,y,z,t) = \text{Re}\left[-\frac{igA}{\omega} \frac{\cosh k(z+h)}{\cosh kh} e^{ik(x\cos\beta + y\sin\beta) - i\omega t} \right], \tag{27}$$

278   where β is the wave heading angle measured from the positive x-direction, and k is the
279   wavenumber. By taking the derivative with respect to time t, the wave-particle velocity in the space
280   can be deduced as

$$U(x,y,z,t) = \frac{\partial \Phi}{\partial x} = \frac{gkA\cos\beta}{\omega} \frac{\cosh k(z+h)}{\cosh kh} \cos[k(x\cos\beta + y\sin\beta) - \omega t], \tag{28}$$

$$V(x, y, z, t) = \frac{\partial \Phi}{\partial y} = \frac{gkA \sin \beta}{\omega} \frac{\cosh k(z + h)}{\cosh kh} \cos[k(x \cos \beta + y \sin \beta) - \omega t], \qquad (29)$$

$$W(x, y, z, t) = \frac{\partial \Phi}{\partial z} = \frac{gkA \sinh k(z + h)}{\omega} \frac{1}{\cosh kh} \sin[k(x \cos \beta + y \sin \beta) - \omega t], \qquad (30)$$

where U, V, and W represent the fluid velocity $\vec{V}_w$ in x, y, and z-direction, respectively. In irregular waves, the above three components can be finally derived as

$$U(x, y, z, t) = \sum_{i=1}^{N} \frac{gk_i A_i \cos \beta}{\omega_i} \frac{\cosh k_i(z + h)}{\cosh k_i h} \cos[k_i(x \cos \beta + y \sin \beta) - \omega_i t + \varepsilon_i], \qquad (31)$$

$$V(x, y, z, t) = \sum_{i=1}^{N} \frac{gk_i A_i \sin \beta}{\omega_i} \frac{\cosh k_i(z + h)}{\cosh k_i h} \cos[k_i(x \cos \beta + y \sin \beta) - \omega_i t + \varepsilon_i], \qquad (32)$$

$$W(x, y, z, t) = \sum_{i=1}^{N} \frac{gk_i A_i}{\omega_i} \frac{\sinh k_i(z + h)}{\cosh k_i h} \sin[k_i(x \cos \beta + y \sin \beta) - \omega_i t + \varepsilon_i], \qquad (33)$$

where the subscript i represents the ith frequency component, ε_i is a random phase uniformly distributed between 0 and 2π. The ith component of wave amplitude A_i can be calculated from

$$A_i(\omega_i) = \sqrt{2S(\omega_i)\Delta\omega_i}, \qquad (34)$$

where $\Delta\omega_i$ is the bandwidth of the discretized wave angular frequency, and $S(\omega_i)$ represents the local power spectrum of irregular waves at a specific site, e.g., JONSWAP (Joint North Sea Wave Observation Project) spectrum, P-M (Pierson-Moskowitz) spectrum, etc. Note that for the deepwater case, the ratio of two hyperbolic functions degrades to the exponential function e^{kz} in Eqs. (27) ~ (30) and $e^{k_i z}$ in Eqs. (31) ~ (33).

5. Validation of the Time-Domain Hybrid Panel-Stick Method

A model experiment was carried out in the towing tank (65m length, 5m width, and 7m depth) of RIAM, Kyushu University. The purpose of the experiment was to check the hydrodynamic performance of the platform and provide a benchmark database for the validation of the numerical code. The platform test model was of 1/50 scale, with a displacement of 0.01693 m³. Each catenary mooring line in the model experiment was substituted by a spring that had an equivalent stiffness to the linearized stiffness of the mooring line. All the springs were anchored to a movable steel frame, which was specifically set for the arrangement of the mooring layout (Figure 4). Two high-speed digital cameras (DITECT HAS-L1™, 1280×1024 pixel, 50fps) are set aside the towing tank, and three yellow spherical markers are set atop the rotor plate for the motion capturing during the experiment.

Before the tank test, the camera system was calibrated by a cubic steel frame with eight spherical markers respectively set at its vertices. The positions of the eight markers in the user-defined coordinate system and two photos of the cubic steel frame from the respective view of each camera were input to the DippMotionPro3D ™ software that was used for processing the camera-recorded videos. When the tank test started, the wind and the waves could be generated and therefore caused the floating platform to oscillate. The platform motion was captured via the movements of the three markers, respectively, by the two monitoring cameras. After the completion of the tank test, the DippMotionPro3D ™ software was used to analyze the videos and calculate the motion time histories of the three markers. Thereby, any point on the floating platform could be calculated based on its relative position to the three markers.
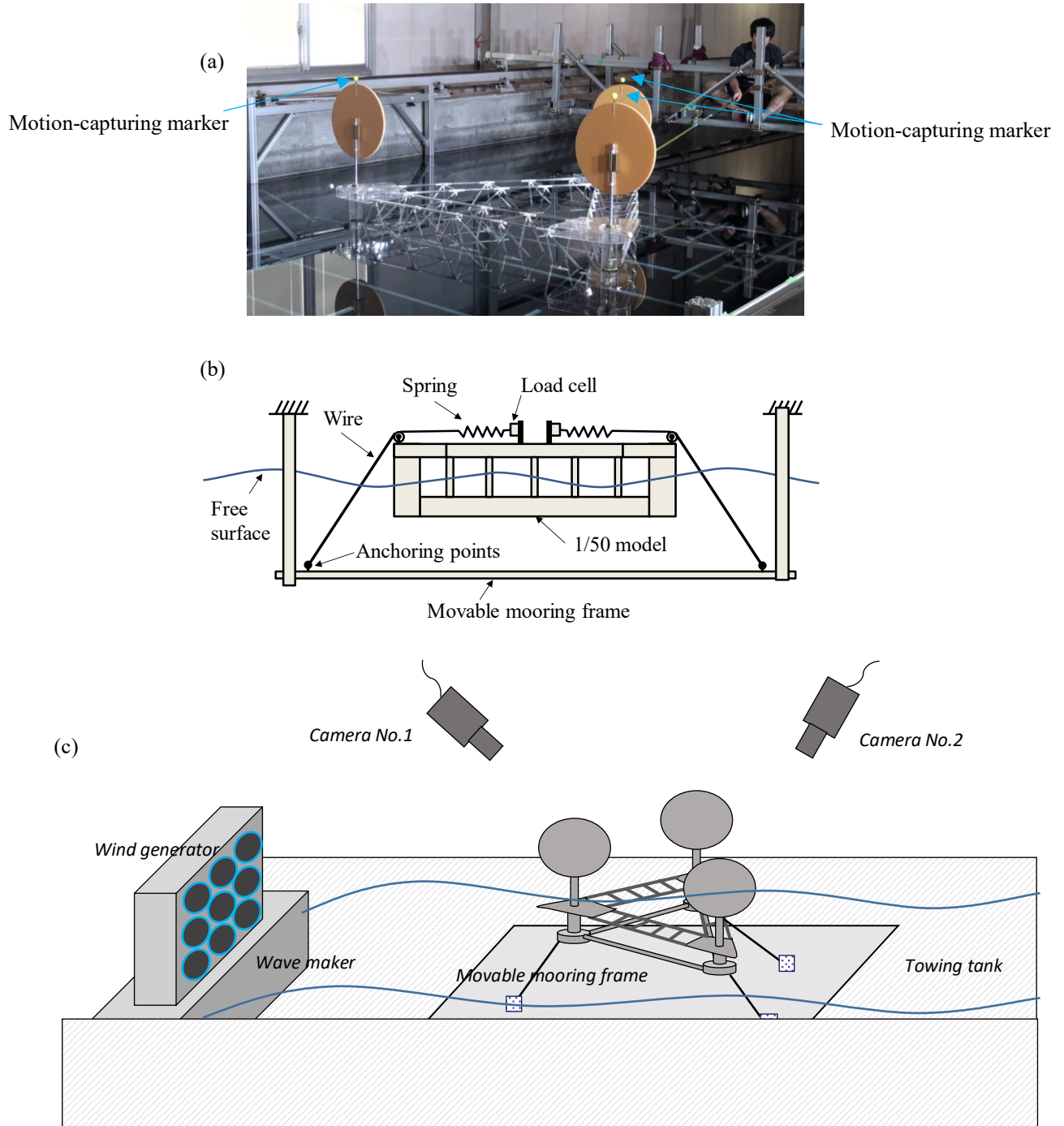
Figure 4. (a) Photo of the experimental model; and a sketch of the experimental setup: (b) tank cross-sectional view, (c) side view.

To validate the preceding hybrid panel-stick time-domain method, the wind was not taken into consideration in either the experiment or the numerical model. The experimental conditions of incident regular waves are given in Table 3. In the numerical model, the wavelengths of the incident regular waves range from $0.05L$ to $7.0L$ (L is the characteristic length of the triangular platform), and the time step is $T/100$ (T is the wave period). The numerical results of the present time-domain method are compared with the frequency-domain results as well as the experimental in Figure 5 and Figure 6. For the fairness between the numerical models, in the frequency-domain model, only the incident waves are considered for the wave kinematics in order to be consistent with Eqs. (27)~(30) of the time-domain model. This means that the wave field is considered not to have been disturbed

326 by the diffracted waves. In general, good agreements can be found between the simulation results
327 and the experiment data. However, an exception occurs in the heave motion that the experimental
328 data are a bit lower than the numerical simulations (when $\lambda/L > 5.0$), while the latter two tend to
329 approach unity with the increase of λ/L. Newman (1999) proved theoretically that in the long-
330 wavelength regime, the heave RAO should approach unity, which in general agrees with the
331 numerical results in Figure 5(b) and Figure 6(c). Moreover, the discrepancies between the frequency-
332 domain and the time-domain results for the heave motion prove the sensitivity of numerical models
333 within this resonant region. When wave heading is 90 deg, the platform is mainly excited in the sway
334 direction. Therefore the motion RAO in surge is small, and the respective measuring error using the
335 experimental facility is larger, which is acceptable and within expectation.

336

Table 3 Experimental conditions of incident regular waves

Wave Period (sec)	Wave Length (m)	Wave Height (cm)	Ratio λ/L
0.71	0.78	1.56	0.5
0.89	1.25	2.50	0.8
1.00	1.56	3.12	1.0
1.10	1.87	3.74	1.2
1.22	2.34	4.68	1.5
1.30	2.65	5.30	1.7
1.41	3.12	6.24	2.0
1.73	4.67	4.68	3.0
2.00	6.24	6.24	4.0
2.12	7.02	7.02	4.5

337

338

339

343

344

345
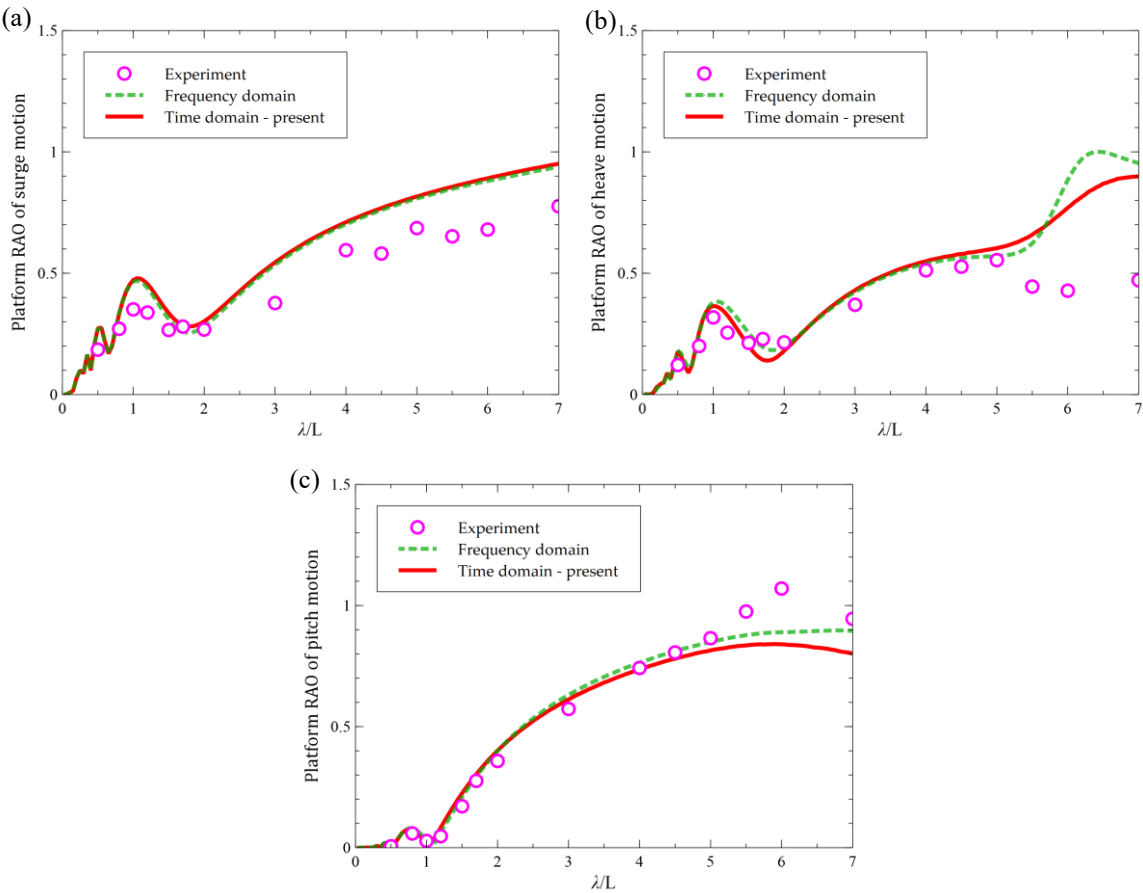
Figure 6. Comparison of the present time-domain method and the model experiment in a regular wave with a heading angle $\beta = 90$ deg: (a) platform surge RAO; (b) sway RAO; (c) heave RAO; (d) roll RAO; (e) pitch RAO; (f) yaw RAO. No wind has been considered in either of the numerical model or the experiment model.

6. Results and Discussion

6.1. Load Cases of the Simulations

In order to analyze the effect of the wave drag force on the motion response of the FWT with numerous truss members, numerical simulations are thereby performed based on the developed time-domain method. Simulations for the FWT in parked status and operating status are carried out

355 separately to discover different phenomenon and reveal different mechanisms. The load cases are
356 shown in Table 4 for the subsequent analysis. For the wind conditions, wind speeds at the rated case
357 (V_{wind} = 11.4 m/s) and an above-rated case (V_{wind} = 15.2 m/s) have been considered. At the above-rated
358 case, the wind turbine applies a collective blade pitch controller. In respect of the wave conditions,
359 unidirectional irregular waves with spectrums in JONSWAP type are considered. As shown in Figure
360 7, simulated spectrums are evaluated from the simulated wave dynamics based on Eq. (27), which
361 are found to be in good agreement with the theoretical spectrums. In addition, for the convenience of
362 the analysis, natural frequencies of the FWT system can be evaluated beforehand with the assist of
363 Hydrostar™ (Chen, 2001) or HAMS© (Liu, 2019), an open-source software package MAP++©
364 (Masciola et al., 2013a, 2013b) and its python wrapper (Masciola, 2015; Liu et al., 2018b), which are
365 listed in Table 5. Based on a heave free decay test performed by CFD in OpenFOAM©, the heave
366 natural period can be calculated from Figure 8 as 17.44 s, which is very much close to the heave
367 natural period from the present method, i.e., $2\pi/0.36$=17.45 s.

368 **Table 4.** Load cases in the subsequent simulations.

Wave/Wind Direction	Wave Conditions		Wind and Rotor Conditions		
	H_s	T_P	V_{wind}	Rotation Speed	Blade Pitch
0 deg	2.44 m	8.10 s	0.0 m/s	0.0 rpm	0.0 deg
			15.2 m/s	12.0 rpm	10.0 deg
90 deg	1.40 m	6.50 s	0.0 m/s	0.0 rpm	0.0 deg
			11.4 m/s	12.0 rpm	0.0 deg

369
370
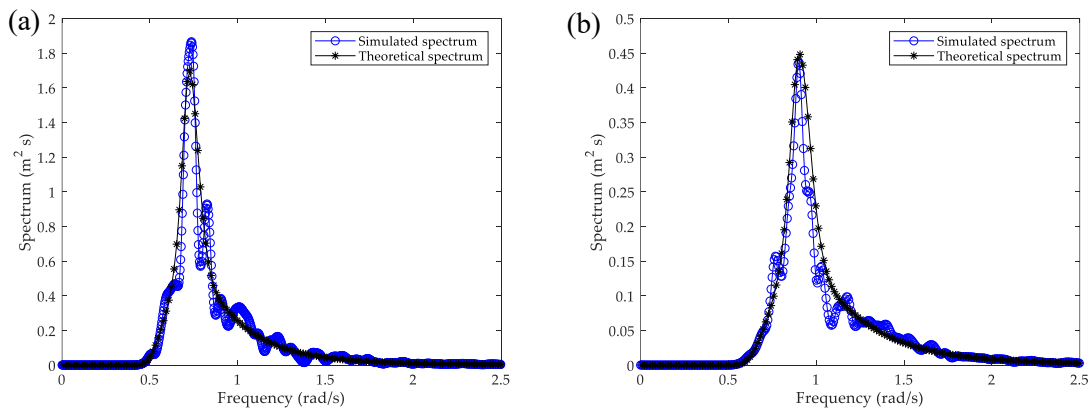
371
372 **Figure 7.** Wave spectrums of unidirectional irregular waves in the simulation. The spectrums are
373 JONSWAP type with a peak enhancement factor γ = 3.3. Left: significant wave height H_s = 2.44 m, peak
374 wave period T_P = 8.1 s; right: significant wave height H_s = 1.4 m, peak wave period T_P = 6.5 s.

375 **Table 5.** Natural frequencies of the FWT system with and without mooring.

Mode	Natural frequencies (rad/s)	
	without mooring	with mooring
Surge	-	0.07
Sway	-	0.07
Heave	0.36	0.36
Roll	0.31	0.32
Pitch	0.32	0.32
Yaw	-	0.09

376

377
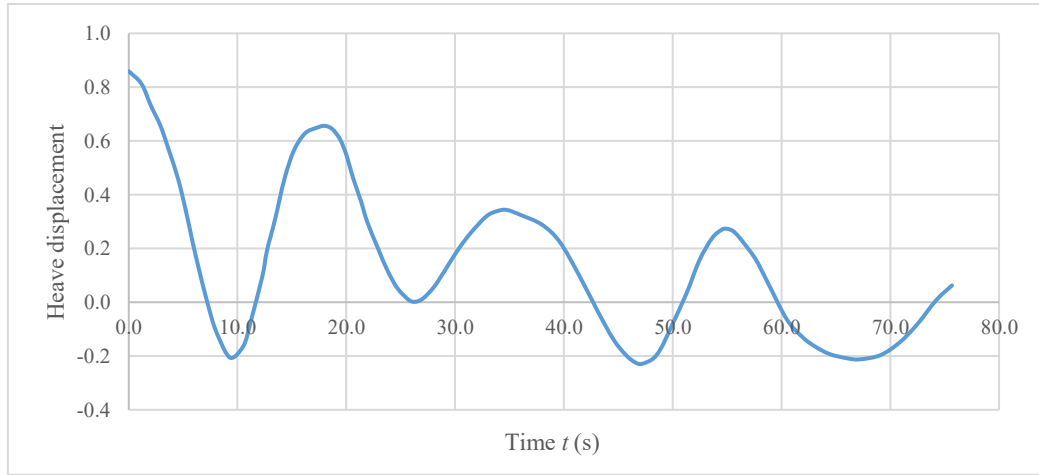
378 **Figure 8.** Free decay test simulated by CFD in OpenFOAM©.

379 *6.2. Motion Response of the Floating Wind Turbine in Parked Status*

380   Since the wave drag force (acting as a certain kind of viscous wave damping) upon an FWT
381 platform is purely hydrodynamic, priority is first given to the motion response of the proposed FWT
382 when it is in parked conditions. There is no wind (in still air) but only waves. For simplicity,
383 misalignment between waves and wind has not been considered, i.e., waves and wind always inflow
384 from the same direction. Responses of the FWT system are simulated using the aforementioned time-
385 domain method. Before the numerical simulation, a convergence test is performed against the time
386 step, as shown in Figure 9. It is found that the size of the time step has little influence on the time-
387 history results. Therefore, a time-step of 0.5 seconds is chosen for each simulation, with a simulation
388 time of 2048 seconds (2 to the power of n, n is an integer) for the sake of the subsequent spectral
389 analysis using FFT (Fast Fourier Transform method). Time series of the platform motions in 6-DOF
390 modes are shown in Figures 10 and 11, respectively, for the wind/wave directions in 0 deg and 90
391 deg.

392
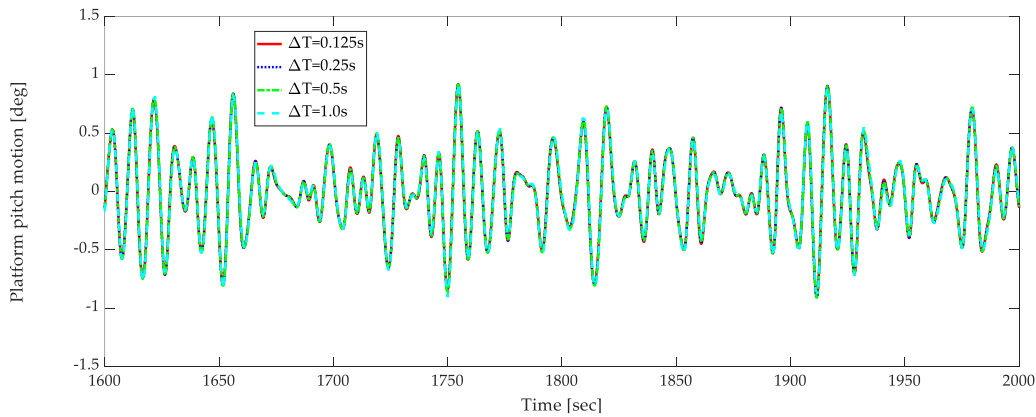
393   **Figure 9.** Convergence test with respect to the time step in the numerical simulations.

394   As shown in Figure 10, since the waves incident from 0 deg (toward the positive *x*-direction),
395 the platform basically displaces in surge, heave, and pitch modes. Figure 10(a), (e), and (i)
396 (particularly (e), and (i)) show that the amplitude of the platform motion response is decreased due
397 to the existence of the viscous effect. The averaged response amplitudes of heave and pitch motions
398 are significantly decreased by respectively 57.85% and 13.92%. Also, with the inclusion of the fluid
399 viscosity, the coupling between different motion DoFs is likely to be enhanced, as can be observed
400 from Figure 10(g) and (k). Based on the 'dat2spec' subroutine of the WAFO© (Wave Analysis for
401 Fatigue and Oceanography) open-source toolbox (Brodtkorb et al., 2000), spectral analysis is
402 performed on the motion response time series in each mode. It is seen that in surge, heave, and pitch,
403 a pure potential flow model without any viscosity leads to a resonant response in correspondence to

404   the natural frequency of the FWT system in that mode. While applying a hybrid panel-stick model
405   can be effective to include the fluid viscosity and hence reduce the fictitious energy of the resonant
406   response. Figure 10(b), (f), and (j) show that the surge, the heave, and the pitch resonances occur at
407   respectively ω = 0.0644 rad/s, ω = 0.3528 rad/s, and ω = 0.2761 rad/s, which are close to respectively
408   the surge natural frequency ω = 0.07 rad/s, the heave natural frequency ω = 0.36 rad/s, and the pitch
409   natural frequency ω = 0.32 rad/s, as displayed in Table 5. Moreover, Figure 10(e) and 6 (i) show that
410   the wave drag force reduces the mean amplitude of the motion time series in heave and pitch,
411   respectively. In addition to the resonant responses, there exists another wave-induced response that
412   is excited by the irregular waves, the peak frequency of which corresponding to the peak frequency
413   of the incident wave spectrum. Figure 10(b), (f), and (j) show that the wave drag force slightly reduces
414   the peak of the wave-induced response. Since the wave incidents from 0 deg, the sway, the roll, and
415   the yaw motions are reasonably in extremely small magnitudes. In Figure 10(g), the existence of
416   viscous damping likely increases the magnitude of the roll motion. That is because, without viscous
417   damping, the roll motion should be almost zero. In contrast, with the existence of viscous damping,
418   which can be viewed as an equivalent to a damping matrix, the roll motion is slightly disturbed by
419   the motions in other modes such as heave, etc. However, since the values are almost negligible, it is
420   hard to draw significant conclusions based on these limited results and, therefore, should be
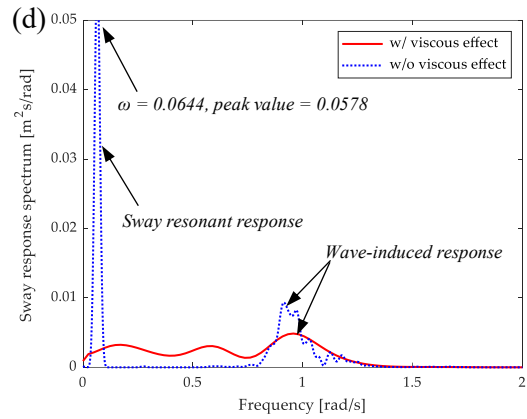421   considered further.
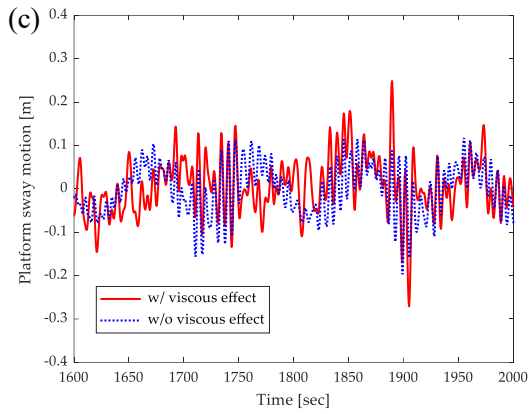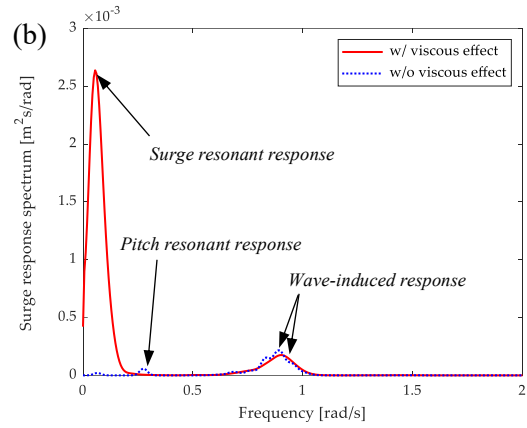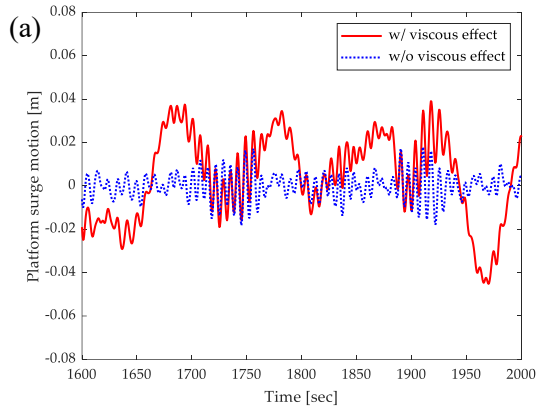422

423

424

425

426

427

428
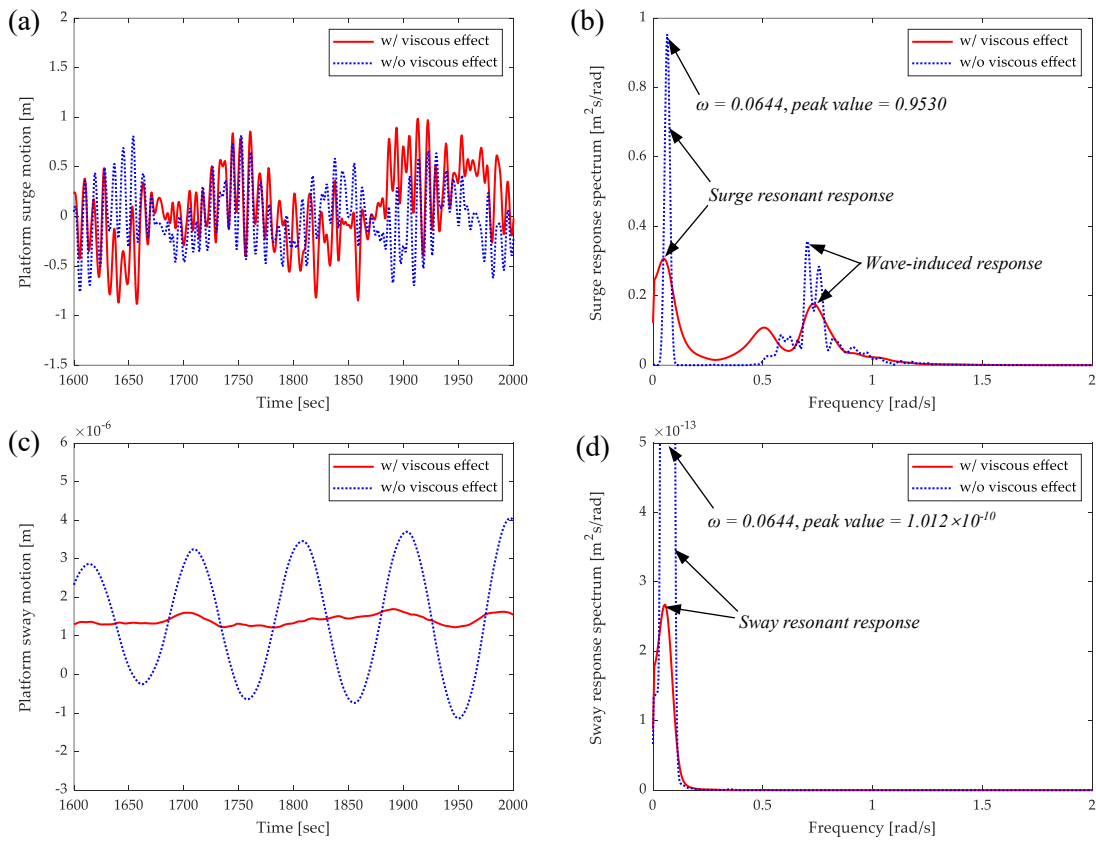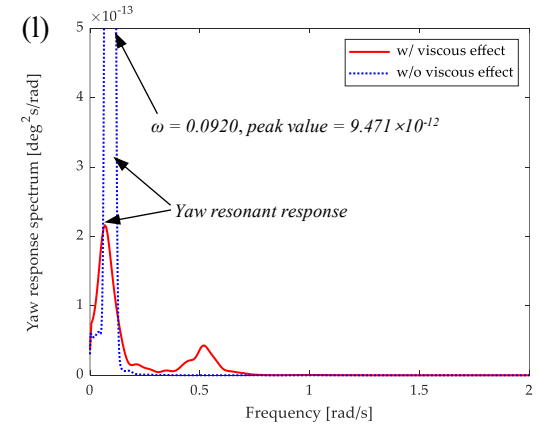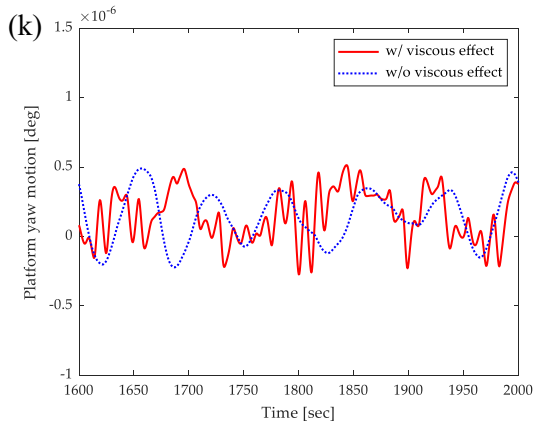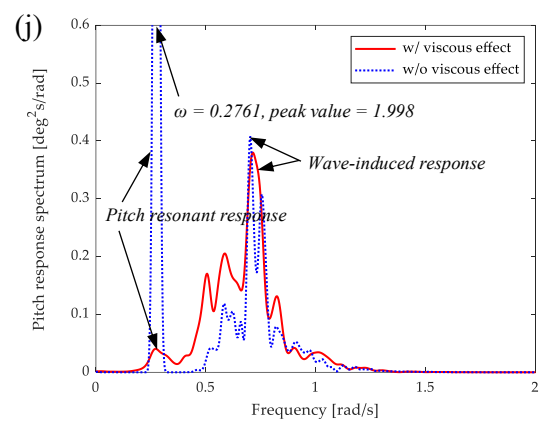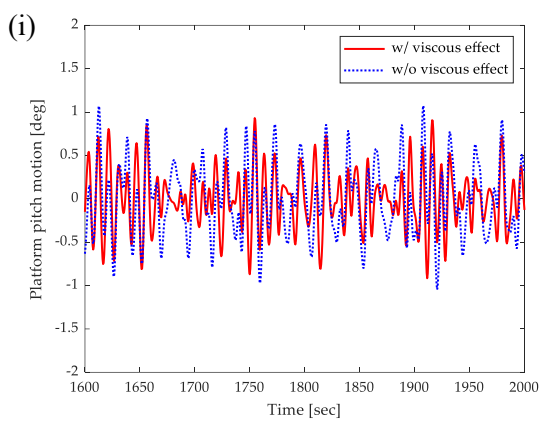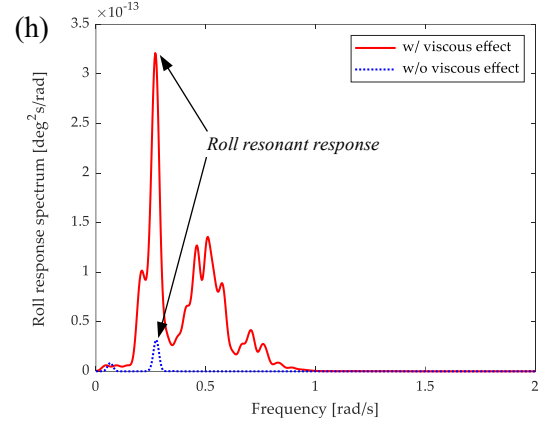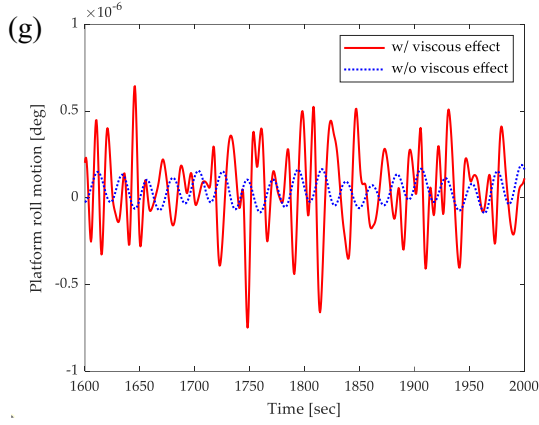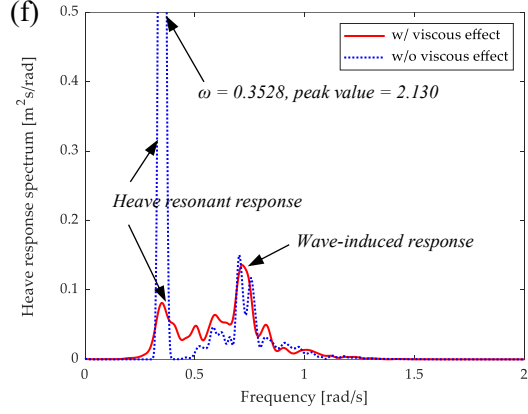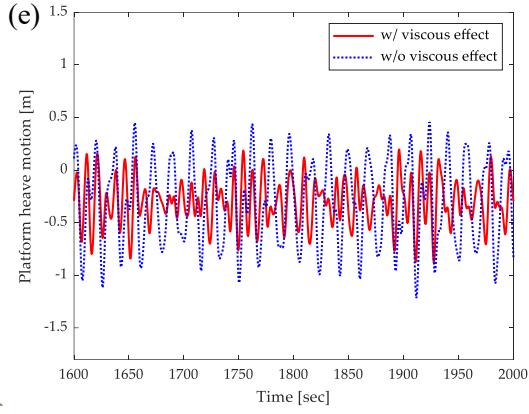
429 **Figure 10.** Time history of the FWT and the spectral analysis. The environmental conditions in the
430 numerical model: no wind (wind speed $V_{wind} = 0$ m/s); unidirectional irregular waves (significant wave
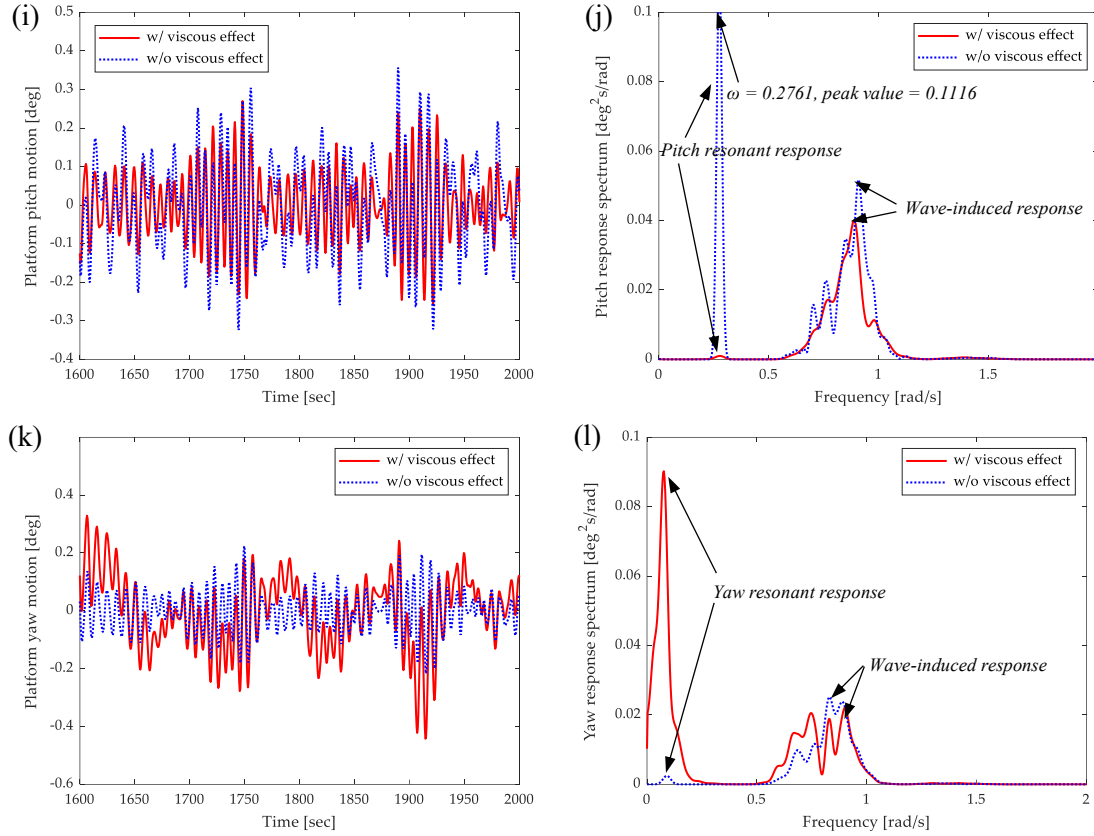431 height $H_s = 2.44$ m, peak wave period $T_P = 8.1$ s, wave heading angle $\beta = 0$ deg).

432

433

434

435
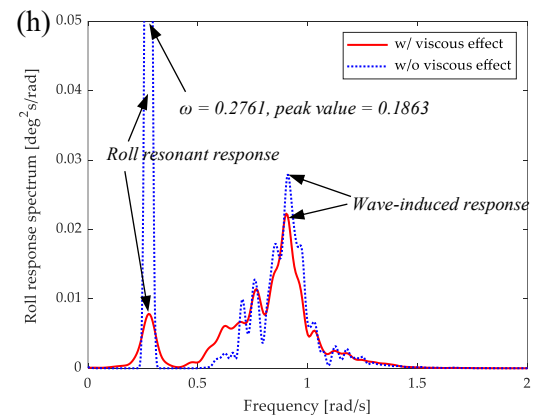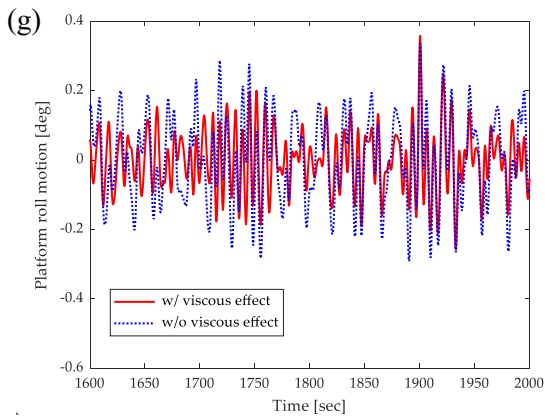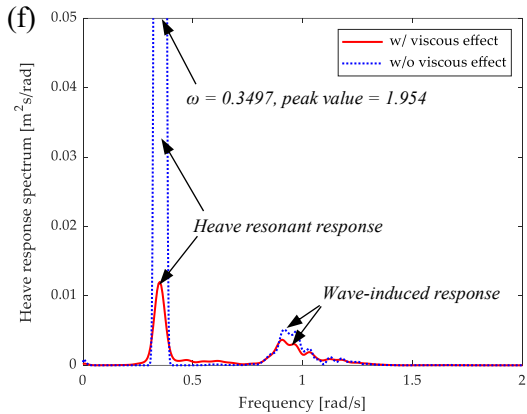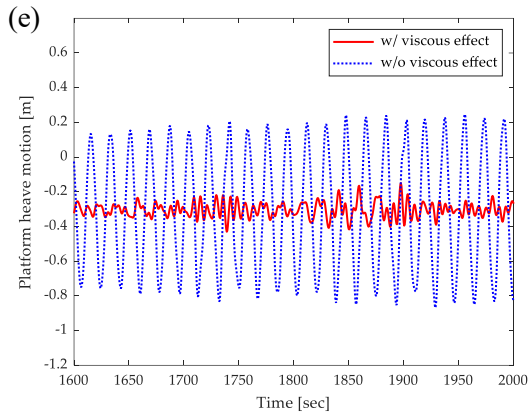
Figure 11. Time history of the FWT and the spectral analysis. The environmental conditions in the numerical model: no wind (wind speed $V_{\text{wind}} = 0\,\text{m/s}$); unidirectional irregular waves (significant wave height $H_s = 1.4$ m, peak wave period $T_P = 6.5$ s, wave heading angle $\beta = 90$ deg).

Figure 11 shows the motion time series of the FWT when the waves incident from the 90 deg direction. The platform displaces basically in sway, heave, roll, and yaw, while the pitch motion is strongly coupled with the heave motion, as shown in Figure 11(c), (e), (g), (i) and (k). Figure 11(a) shows that the surge motion is also affected by enhancing the motion response of the resonant frequency component. Figure 11(d), (f), (h) and (j) show that the sway, the heave, the roll and the pitch resonances occur at respectively $\omega = 0.0644$ rad/s, $\omega = 0.3497$ rad/s, $\omega = 0.2761$ rad/s and $\omega = 0.2761$ rad/s, which are close to respectively the sway natural frequency $\omega = 0.07$ rad/s, the heave natural frequency $\omega = 0.36$ rad/s, the roll natural frequency $\omega = 0.32$ rad/s and the pitch natural frequency $\omega = 0.32$ rad/s, as displayed in Table 5. With the existence of the fluid viscosity, the resonances are effectively reduced, which can be known from the red-line simulation results with the wave viscous damping. Moreover, similar to that has been found in Figure 10, the viscous wave effect decreases slightly the peak of the wave-induced response excited by the irregular waves with a JONSWAP spectrum, as shown in Figure 11(d), (f), (h), (j) and (l). Worth noting is that the presence of the fluid viscosity is likely to enhance the coupling between the motions in different DoFs, which can be observed from the resonant response energy of the yaw response spectrum, as shown in Figure 11(l).

*6.3. Motion Response of the Floating Wind Turbine in Operation*

After knowing the motion response characteristics of the FWT in the still-air condition, it is interesting to know what the characteristics will be like if the wind is involved as well. In this section, therefore, simulations are performed for the FWT when it is in operation. To give a clear explanation, turbulent winds and misalignments between wind and waves are not considered here. In other words, the wind steadily comes from the same direction as the waves. Each of the simulations lasts

463 for 2048 seconds with a time step of 0.5 seconds. Time series of the platform motions in 6-DoF modes
464 are shown in Figures 12 and 13, respectively, for the wind/wave directions in 0 deg and 90 deg.
465   Figure 12 shows the platform motion time histories and the spectral analysis when the waves
466 and the wind come from the positive x-direction. Similar to Figure 10, the platform displaces in surge,
467 heave, and pitch, as shown in Figure 12(a), (e) and (i). It is found that, in general, the motion
468 amplitudes in almost all the DoFs have been decreased by the inclusion of the fluid viscosity in the
469 presence of wind. Again, the same resonant frequencies are obtained with the aid of the WAFO©
470 toolbox, which are in coincidence with the natural frequencies in Table 5. Worth noting is that the
471 resonance in the surge motion without the fluid viscosity can be excited prominently in the presence
472 of the wind. That is to say, the one component of the surge motion (which consists of an infinite set
473 of components with different frequencies) with a frequency equivalent to that of the surge resonance
474 ($\omega = 0.0644$ rad/s) are particularly excited due to the existence of the wind. This phenomenon can be
475 confirmed again by the spectral analysis of the pitch motion time series, as given in Figure 12(j). In
476 comparison to Figure 10(j), i.e., the case without wind, there is an additional distinctive resonant
477 response with a peak at the surge resonance frequency ($\omega = 0.0644$ rad/s). It can be known for sure
478 that this peak is induced by the resonant response of the surge motion since the pitch and the surge
479 motions are strongly coupled. However, in the presence of the fluid viscosity, the surge resonant
480 response diminishes, and the pitch resonant response is also significantly reduced, as shown in Figure
481 10(b) and 10(j).
482   The reason why the steady wind excites the surge resonance can be explained as below: (1) In
483 the still-air condition, as shown in Figure 10(a), the equilibrium position of the platform motion is set
484 at the origin of the ground-based global coordinate system. Starting from the equilibrium position,
485 the platform moves with an initial velocity, which is induced by the waves. (2) In the presence of the
486 steady wind, the equilibrium position of the platform surge motion changes to a place having a
487 distance (2.5 m in the present case as shown in Figure 12(a)) from the origin, resulting from the new
488 balance between the actions of the wind thrust force, the wave excitation force and the mooring
489 restoring force. The work that the wind has done to the FWT along the 2.5 m distance increases the
490 total kinetic energy of the platform remarkably and therefore increases the surge velocity of the
491 platform at the equilibrium position. (3) Without the existence of wave viscous damping (much larger
492 than the wave radiation damping at the platform resonant frequency), the amplitude of the platform
493 surge motion can increase to a considerable value. In reality, the existence of wave viscous damping
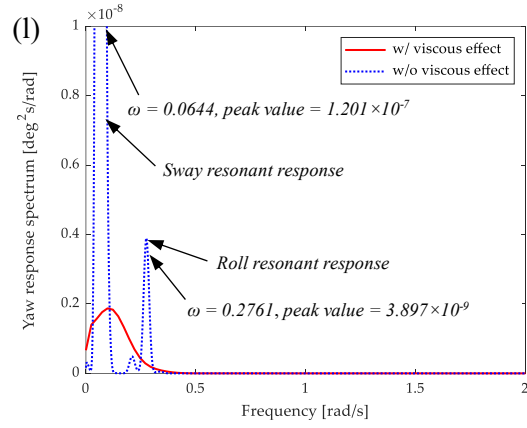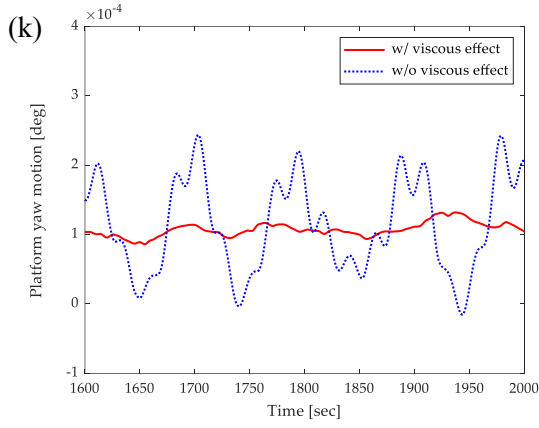494 reduces the amplitude of the platform motion significantly.

495

496

497

498

499

500
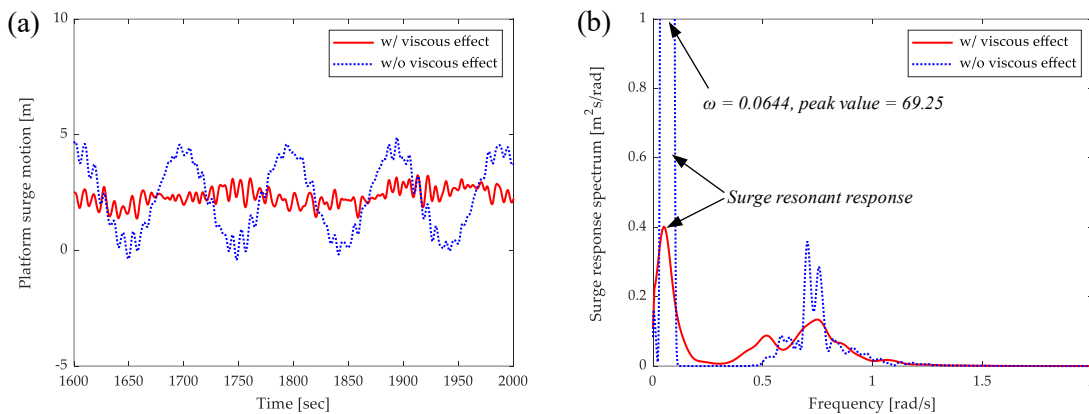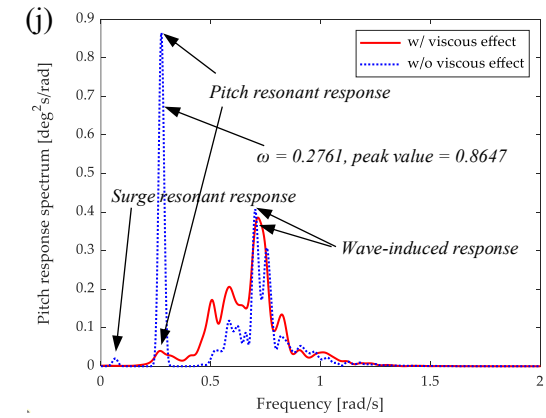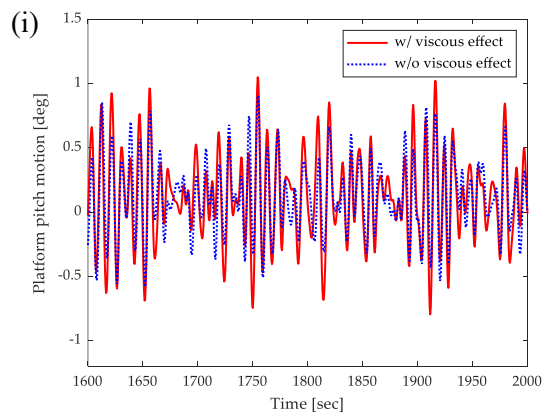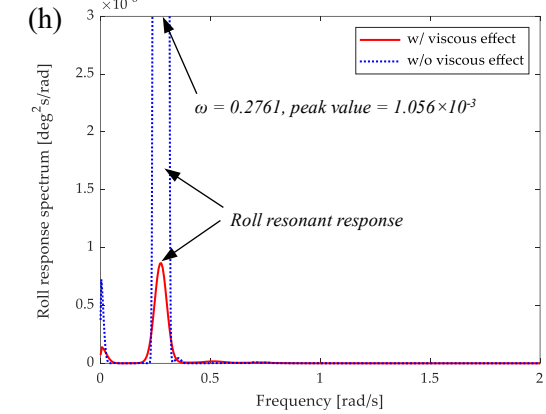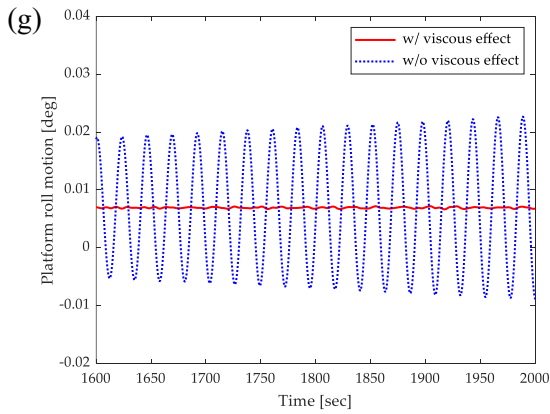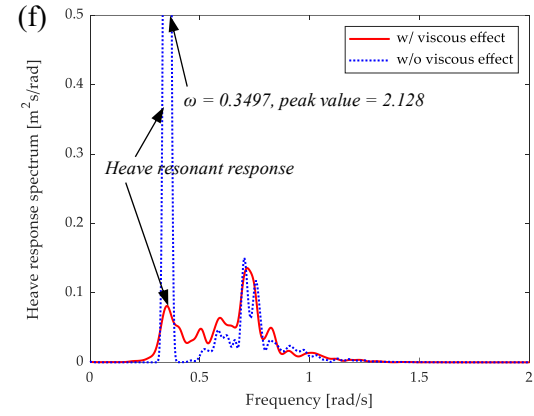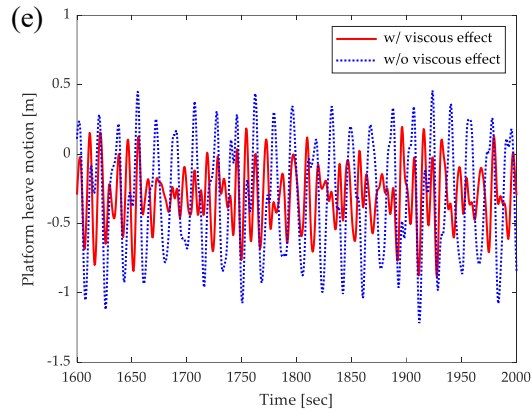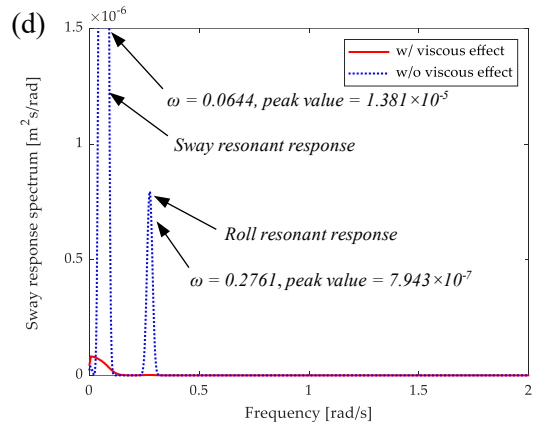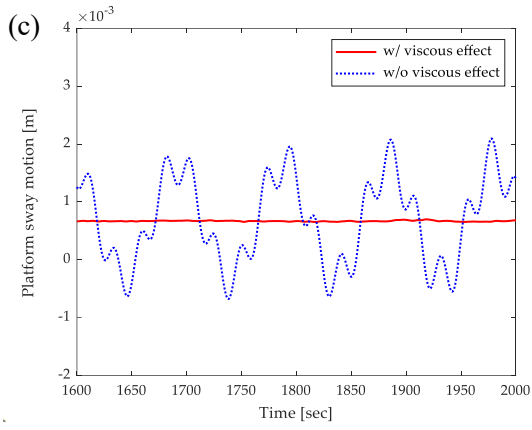
501 **Figure 12.** Time history of the FWT and the spectral analysis. The environmental conditions in the
502 numerical model: steady wind (wind speed V_{wind} = 15.2 m/s, wind direction α = 0 deg); unidirectional
503 irregular waves (significant wave height H_s = 2.44 m, peak wave period T_p = 8.1 s, wave heading angle
504 β = 0 deg).

505

506

507
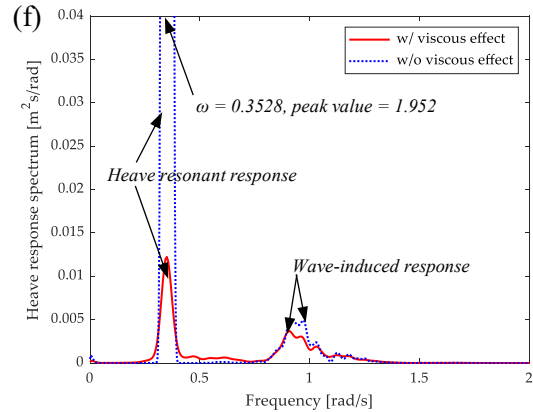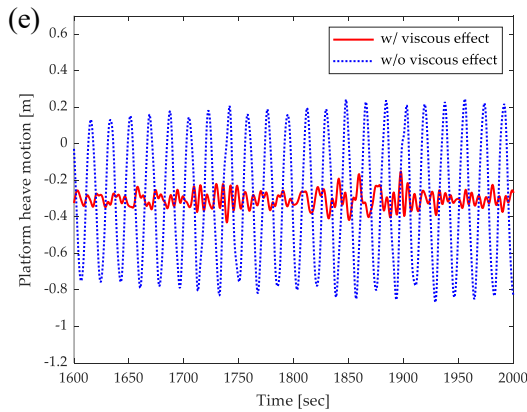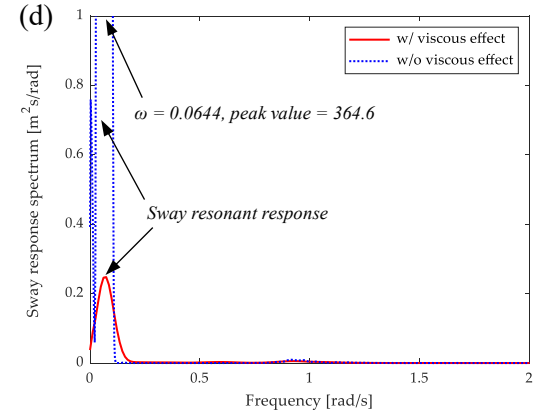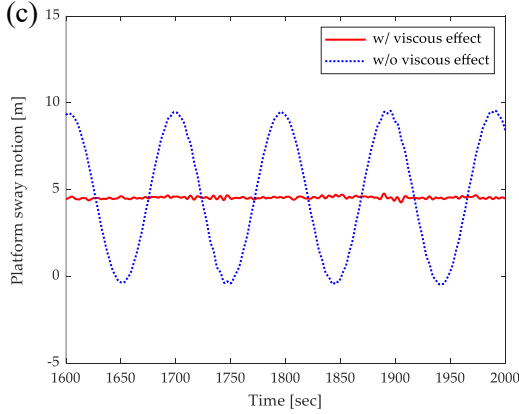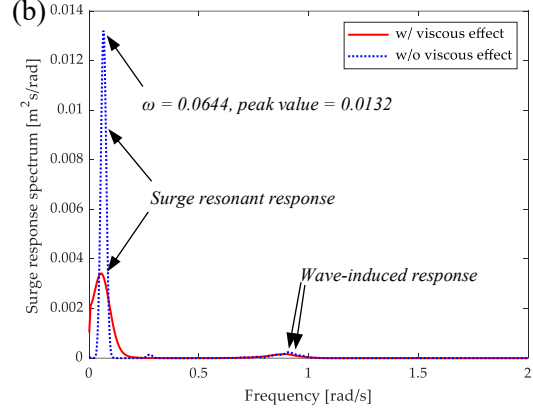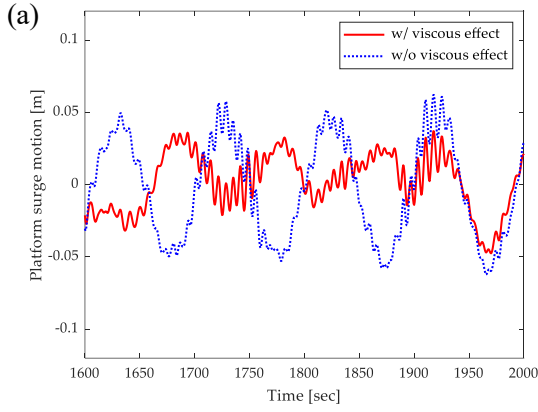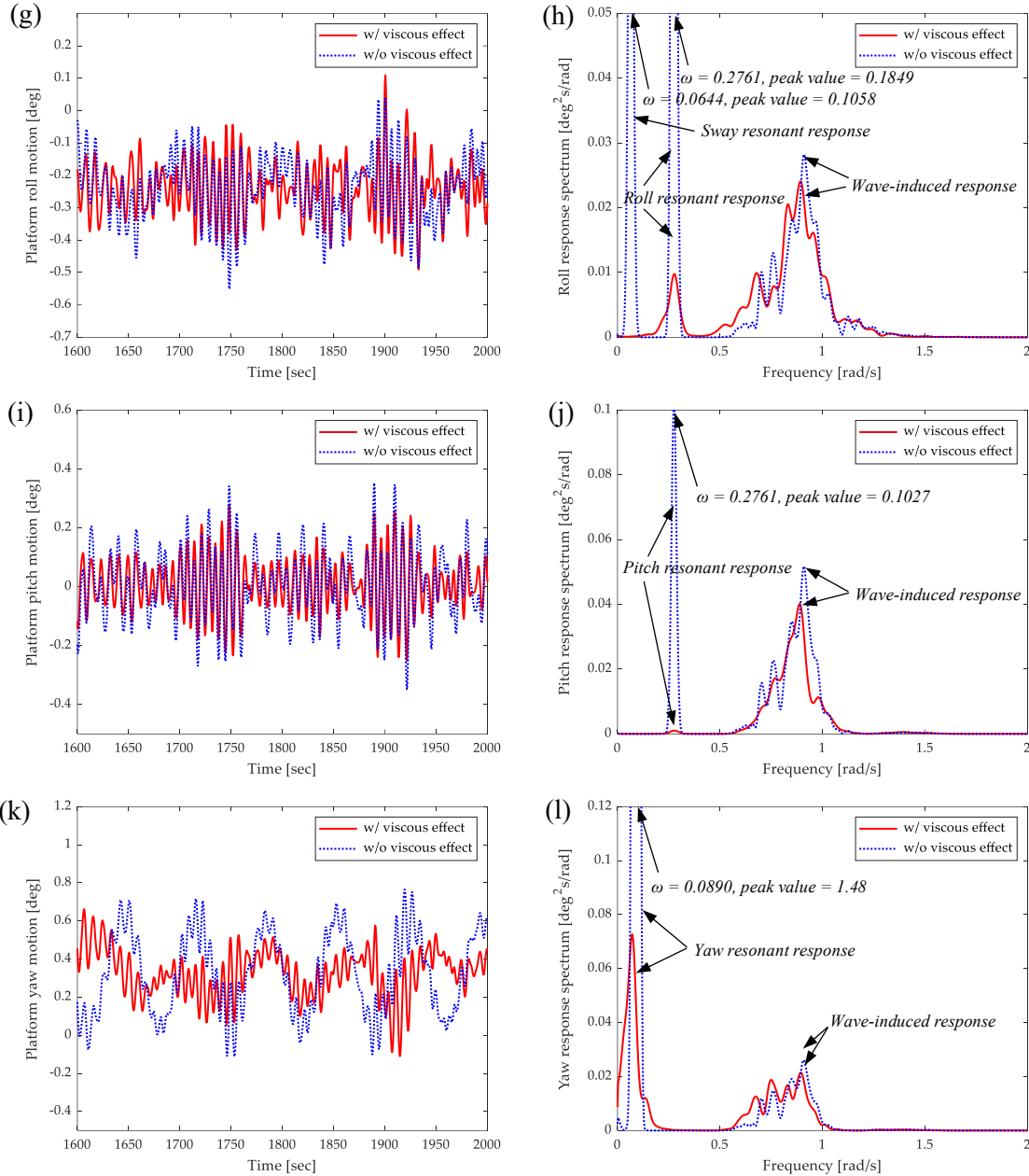
Figure 13. Time history of the FWT and the spectral analysis. The environmental conditions in the numerical model: steady wind (wind speed V_{wind} = 11.4 m/s, wind direction α = 90 deg); unidirectional irregular waves (significant wave height H_s = 1.4 m, peak wave period T_P = 6.5 s, wave heading angle β = 90 deg).

Figure 13 shows the motion time series of the FWT when the waves and the wind come from the 90 deg direction. Similar to Figure 11, the platform displaces basically in sway, heave, roll, and yaw, as well as pitch that is induced by the coupled heave motion, as shown in Figure 13(c), (e), (g), (k) and (i). Figure 13(a) shows that the surge motion is affected as well by enhancing the motion response of the resonant frequency component. Again, the translational sway motion with the assumption of no fluid viscosity is excited particularly at the sway resonant frequency (ω = 0.0644 rad/s), which is close to the natural frequency (ω = 0.07 rad/s) of the FWT system in the sway mode, as shown in Figure 13(c) and 13(d). The reason for the excitation of the sway resonant response is analogous to that of the surge in Figure 12(a) and (b). As a consequence, a resonance at the sway resonant frequency (ω = 0.0644 rad/s) is also excited in the platform roll motion, which can be confirmed from Figure 13(g) and 13(h). It is because of the strong coupling between the platform sway motion and the roll

526 motion. With the existence of the fluid viscosity, the amplitudes of these platform motion time series
527 are effectively decreased, as well as the resonant response peaks in their spectrums.

528 **7. Conclusions**

529   This paper presents a time-domain method for modeling the dynamics of an FWT with multiple
530 rotors on the deck of a semi-submersible floating platform. It is particularly noticed that the floating
531 foundation is a truss structure consisting of many slender braces. Such slim members can bring a
532 significant effect of the viscous wave damping, which is caused by the wave drag force upon those
533 members.

534   A systematic methodology of modeling such a floating truss structure is established based on
535 the proposed time-domain hybrid panel-stick method, combining the potential flow theory for large-
536 diameter structures with the Morison strip method for small-diameter structures. In the meantime,
537 an efficient tool has been developed to deal with a set of slender cylindrical members in arbitrary
538 lengths, diameters, orientations, and locations. The tool includes a stick mesh generator and a
539 Morison dynamic solver. The Morison dynamic solver has been incorporated into the time-domain
540 solver for the FWT dynamics. The developed methodology and software are then applied to an FWT
541 developed in Kyushu University. It is validated with an experiment in regular waves in the wave
542 tank of RIAM, Kyushu University. The simulation results are in good agreement with the
543 experimental data, confirming the validity of the developed method for the FWT. Further numerical
544 simulations are carried out under a set of wind and wave conditions. Comparisons are made between
545 the parked wind turbine and the operating wind turbine and between simulations with and without
546 the viscous damping.

547   It is found that in all cases of conditions without consideration of the wave drag force, the
548 platform has a resonant response occurring at the resonant frequency of each DoF. The resonant
549 frequencies are close to the natural frequencies of the FWT system with moorings. In addition to the
550 resonant response, the wave-induced response is always excited, whose peak frequency coincides
551 with that of the incident wave spectrum. However, in the presence of viscous damping, the peak
552 value of wave-induced response can be slightly reduced. With the effect of viscous damping, which
553 is evaluated by the Morison dynamic solver, the resonant response of each DoF can be suppressed. It
554 means that the energy of resonant response dissipates with the fluid viscosity. In the presence of
555 steady wind, the translational surge or sway motion can be significantly excited at its resonance
556 frequency, in comparison to the case when the wind turbine is parked. It is mainly due to the work
557 that the wind has done to the FWT, which enhances remarkably the total kinetic energy of the
558 platform and, therefore, increases the translational velocity of the platform in the surge or sway DoF
559 at the equilibrium position. An additional resonant response due to the sway or surge resonance is
560 excited as well in the rotational platform motion of the roll or pitch DoF. It can be attributed to the
561 strong couplings between the sway and the roll motions and between the surge and the pitch
562 motions. These findings are believed to be of great importance to the design and operation of such
563 FWT systems.

571 **Conflicts of Interest:** No potential conflict of interest was reported by the authors.

572 **Nomenclature**

BEM	Boundary Element Method
BEMT	Blade Element Momentum Theory

CFD	Computational Fluid Dynamics
DOF	Degree of Freedom
FWT	Floating Wind Turbine
HAMS	Hydrodynamic Analysis of Marine Structures
JONSWAP	Joint North Sea Wave Observation Project
MAP++	Mooring Analysis Program
MSL	Mean Sea Level
N-S	Navier-Stokes
P-M	Pierson-Moskowitz
RAO	Response Amplitude Operator
RIAM	Research Institute for Applied Mechanics
TLP	Tension Leg Platform
WAFO	Wave Analysis for Fatigue and Oceanography
WINFLO	Wind turbine with INnovative design for Floating Lightweight Offshore

573

References

1. Bae, Y. H., Kim, M. H., 2014. Coupled dynamic analysis of multiple wind turbines on a large single floater. *Ocean Engineering*, 92, 175-187.

2. Barthelmie R., Hansen K., Frandsen S., Rathmann O., Schepers J., Schlez W., Phillips J., Rados K., Zervos A., Politis E., Chaviaropoulos P., 2009. Modelling and measuring flow and wind turbine wakes in large wind farms offshore. *Wind Energy* 12(5):431-44.

3. Barthelmie R., Larsen G., Frandsen S., Folkerts L., Rados K., Pryor S., Lange B., Schepers G., 2006. *Journal* Comparison of wake model simulations with offshore wind turbine wake profiles measured by sodar. *of Atmospheric and Oceanic Technology* 23(7):888-901.

4. Bayati, I., Jonkman, J., Robertson, A., Platt, A., 2014. The effects of second-order hydrodynamics on a semi-submersible floating offshore wind turbine. In: *Journal of Physics: Conference Series* (Vol. 524, No. 1, p. 012094). IOP Publishing.

5. Benitz M., Lackner M., Schmidt D., 2015. Hydrodynamics of offshore structures with specific focus on wind energy applications. *Renewable and Sustainable Energy Reviews* 44:692-716.

6. Boulluec M. Le, Ohana J., Martin A., Houmard A., 2013. Tank testing of a new concept of floating offshore wind turbine, in: *Proc. 32nd International Conference on Ocean, Offshore and Arctic Engineering*, Nantes, France.

7. Brodtkorb, P., Johannesson, P., Lindgren, G., Rychlik, I., Rydén, J., Sjö, E., 2000. WAFO - a Matlab toolbox for analysis of random waves and loads. *Proceedings of the 10th International Offshore and Polar Engineering Conference*, Seattle.

8. Chen X., 2004. Hydrodynamics in offshore and naval applications - Part I. In: *Proc. Of the 6th Intl. Conf. Hydrodynamics*, Perth, Australia.

9. Faltinsen O., 1993. *Sea loads on ships and offshore structures*. Cambridge: Cambridge University Press.

10. Goupee A., Koo B., Kimball R., Lambrakos K., Dagher H., 2014. Experimental comparison of three floating wind turbine concepts. *Journal of Offshore Mechanics and Arctic Engineering* 136(2): 020906.

11. Hansen M., 2015. *Aerodynamics of wind turbines*. Routledge.

12. Hu C., Sueyoshi M., Liu C., Liu Y., 2014. Hydrodynamic analysis of a semi-submersible type floating wind turbine. *Journal of Ocean and Wind Energy* 1(4): 202-208.

13. Ishihara, T., Zhang, S., 2019. Prediction of dynamic response of semi-submersible floating offshore wind turbine using augmented Morison's equation with frequency dependent hydrodynamic coefficients. *Renewable Energy*, 131, 1186-1207.

14. Jensen, N., 1983. *A note on wind generator interaction*. Technical Report from the Risø National Laboratory (Risø-M-2411), Roskilde, Denmark.

15. Jonkman, J., 2007. *Dynamics Modeling and Loads Analysis of an Offshore Floating Wind Turbine*; University of Colorado at Boulder: Boulder, CO, USA; Volume 3, ISBN 0070378460.

16. Jonkman J., 2009. Dynamics of offshore floating wind turbines—model development and verification. *Wind Energy* 12(5):459-92.

17. Karimirad, M., Michailides, C., 2015. V-shaped semi-submersible offshore wind turbine: An alternative concept for offshore wind technology. *Renewable Energy*, 83, 126-143.

612 18. Karimirad, M., Michailides, C., 2016. V-shaped semi-submersible offshore wind turbine subjected to
613   misaligned wave and wind. *Journal of Renewable and Sustainable Energy*, 8(2), 023305.
614 19. Katic, I., Højstrup, J., Jensen, N., 1986. *A simple model for cluster efficiency*. In European Wind Energy
615   Association Conference and Exhibition.
616 20. Kim, H. C., Kim, K. H., Kim, M. H., Hong, K., 2017. Global performance of a KRISO semi-submersible
617   multiunit floating offshore wind turbine: Numerical simulation vs. model test. *International Journal of
618   Offshore and Polar Engineering*, 27(01), 70-81.
619 21. Koch, C., Lemmer, F., Borisade, F., Matha, D., Cheng, P. W., 2018. Validation of INNWIND. EU scaled
620   model tests of a semi-submersible floating wind turbine. *International Journal of Offshore and Polar
621   Engineering*, 28(01), 54-64.
622 22. Kvittem, M. I., Bachynski, E. E., Moan, T., 2012. Effects of hydrodynamic modelling in fully coupled
623   simulations of a semi-submersible wind turbine. *Energy Procedia*, 24, 351-362.
624 23. Leblanc L., Petitjean F., Roy F., Chen X., 1993. A mixed panel-stick hydrodynamic model applied to fatigue
625   life assessment of semi-submersibles. *Proceedings of 12th International Conference on Ocean, Offshore and Arctic
626   Engineering*, Glasgow, Scotland.
627 24. Ledru, R., Le Cunff, C., Heurtier, J. M., Perdrizet, T., Poirette, Y., 2014. Influence of Hydrodynamic
628   Modeling Assumptions on Floating Wind Turbine Behaviour. *Proceedings of 33rd International Conference on
629   Ocean, Offshore and Arctic Engineering*.
630 25. Li B, Liu K, Yan G, Ou J., 2011. Hydrodynamic comparison of a semi-submersible, TLP, and Spar: numerical
631   study in the South China Sea environment. *J. Mar. Sci. Appl.* 10: 306–14.
632 26. Li, L., Gao, Y., Hu, Z., Yuan, Z., Day, S., Li, H., 2018. Model test research of a semi-submersible floating
633   wind turbine with an improved deficient thrust force correction approach. *Renewable energy*, 119, 95-105.
634 27. Li, Y., Teng, B., 2002. *Wave action on maritime structures (in Chinese)*. Ocean Press, Beijing.
635 28. Li, Y., Yu, Y. H., 2012. A synthesis of numerical methods for modeling wave energy converter-point
636   absorbers. *Renewable and Sustainable Energy Reviews*, 16(6), 4352-4364.
637 29. Liu, Y., Hu, C., Sueyoshi, M., Yoshida, S., Honda, Y., Ohya, Y., 2014. Time domain simulation of a semi-
638   submersible type floating wind turbine. *Proceedings of 24th International Ocean and Polar Engineering
639   Conference*, Busan, Korea.
640 30. Liu, Y., Li, S., Yi, Q., Chen, D., 2016a. Developments in semi-submersible floating foundations supporting
641   wind turbines: A comprehensive review. *Renew. Sustain. Energy Rev.* 60: 433–449.
642 31. Liu Y., Hu C., Sueyoshi M., Iwashita H., Kashiwagi M., 2016b. Motion response prediction by hybrid panel-
643   stick models for a semi-submersible with bracings. *Journal of Marine Science and Technology* 21(4):742-57.
644 32. Liu Y., Yoshida S., Hu C., Sueyoshi M., Sun L., Gao J., Cong P., He G., 2018a. A reliable open-source package
645   for performance evaluation of floating renewable energy systems in coastal and offshore regions. *Energy
646   Conversion and Management* 174: 516-536.
647 33. Liu, Y., Yoshida, S., Yamamoto, H., Toyofuku, A., He, G., Yang, S. 2018b. Response Characteristics of the
648   DeepCwind Floating Wind Turbine Moored by a Single-Point Mooring System. *Applied Sciences*, 8(11),
649   2306.
650 34. Liu, Y., Li, S., Chan, P. W., Chen, D., 2018c. On the Failure Probability of Offshore Wind Turbines in the
651   China Coastal Waters Due to Typhoons: A Case Study Using the OC4-DeepCwind Semisubmersible. *IEEE
652   Transactions on Sustainable Energy*, 10(2), 522-532.
653 35. Liu Y., 2019. HAMS: A Frequency-Domain Preprocessor for Wave-Structure Interactions—Theory,
654   Development, and Application. *Journal of Marine Science and Engineering*, 7(3), 81.
655 36. Masciola, M., 2013a. *Instructional and Theory Guide to the Mooring Analysis Program*. NREL. Available online:
656   https://nwtc. nrel. gov/system/files/MAP_v0, 87 (accessed on 25 Feb 2019).
657 37. Masciola, M.; Jonkman, J.; Robertson, A., 2013b. Implementation of a multi-segmented, quasi-static cable
658   model. In *Proceedings of the Twenty-third International Offshore and Polar Engineering Conference*, Anchorage,
659   AK, USA.
660 38. Masciola M., 2015. MAP++ Python Wrapper.
661   https://map-plus-plus.readthedocs.io/en/latest/python_example.html (accessed on 13 May 2020).
662 39. Moriarty P., Hansen A., 2005. *AeroDyn theory manual*. National Renewable Energy Lab., Golden, CO (US).
663 40. Nematbakhsh, A., Bachynski, E. E., Gao, Z., Moan, T., 2015. Comparison of wave load effects on a TLP
664   wind turbine by using computational fluid dynamics and potential flow theory approaches. *Applied Ocean
665   Research*, 53, 142-154.

666 41. Newman J.N., 1999. *Heave response of a semi-submersible near resonance*. Proceedings of 14th International
667 Workshop on Water Waves and Floating Bodies, Port Huron, USA.
668 42. Ran, Z., 2000. *Coupled dynamic analysis of floating structures in waves and currents*. Doctoral dissertation, Texas
669 A&M University.
670 43. Robertson, A., Jonkman, J.M., Masciola, M., Song, H., Goupee, A., Coulling, A., Luan, C., 2014. *Definition of*
671 *the Semisubmersible Floating System for Phase II of OC4*; National Renewable Energy Laboratory (NREL):
672 Golden, CO, USA.
673 44. Robertson, A. N., Wendt, F., Jonkman, J. M., Popko, W., Dagher, H., Gueydon, S., ... & Soares, C. G., 2017.
674 OC5 project phase II: validation of global loads of the DeepCwind floating semi-submersible wind
675 turbine. *Energy Procedia*, 137, 38-57.
676 45. Roddier, D., Cermelli, C., Aubault, A., Weinstein, A., 2010. WindFloat: A floating foundation for offshore
677 wind turbines. *J. Renew. Sustain. Energy 2*: 033104.Sarpkaya T., 2010. *Wave forces on offshore structures*.
678 Cambridge: Cambridge University Press.
679 46. Spera, D., 1994. *Wind Turbine Technology*, ASME Press, New York.
680 47. Tran, T. T., Kim, D. H., 2015. The coupled dynamic response computation for a semi-submersible platform
681 of floating offshore wind turbine. *Journal of wind engineering and industrial aerodynamics*, 147, 104-119.
682 48. Uzunoglu, E., Soares, C. G., 2018. On the model uncertainty of wave induced platform motions and
683 mooring loads of a semi-submersible based wind turbine. *Ocean Engineering*, 148, 277-285.
684 49. Wang, K., Ji, C., Xue, H., & Tang, W., 2016. Fatigue damage characteristics of a semisubmersible-type
685 floating offshore wind turbine at tower base. *Journal of Renewable and Sustainable Energy*, 8(5), 053307.
686 50. Wendt, F. F., Robertson, A., Jonkman, J. M., Hayman, G., 2015. *Verification of new floating capabilities in FAST*
687 *v8*. In 33rd Wind Energy Symposium (p. 1204).
688 51. Wikipedia, 2020a. https://en.wikipedia.org/wiki/Newmark-beta_method (accessed on 8 May 2020).
689 52. Wikiversity,2020b. https://en.wikiversity.org/wiki/Adams-Bashforth_and_Adams-Moulton_methods (acc-
690 essed on 8 May 2020).
691 53. Wikipedia, 2020c. https://en.wikipedia.org/wiki/Runge%E2%80%93Kutta_methods (accessed on 8 May
692 2020).
693 54. Xiang, S., 2007. On the Filon and Levin methods for highly oscillatory integral∫ abf (x) eiωg (x) dx. *Journal*
694 *of computational and applied mathematics*, 208(2), 434-439.
695 55. Zhu, H., Hu, C., Liu, Y., 2016. Optimum design of a passive suspension system of a semi-submersible for
696 pitching reduction. J*ournal of Dynamic Systems, Measurement, and Control*, 138(12), 121003.
697